Loss of *slc39a14* causes simultaneous manganese hypersensitivity and deficiency in zebrafish

Karin Tuschl[1-3,*], Richard J White[4,5], Chintan Trivedi[2], Leonardo E Valdivia[2,6,7], Stephanie Niklaus[8], Isaac H Bianco[9], Chris Dadswell[10], Ramón González-Méndez[10], Ian M Sealy[4,5], Stephan CF Neuhauss[8], Corinne Houart[3], Jason Rihel[2], Stephen W Wilson[2], Elisabeth M Busch-Nentwich[4,5,*]

1 UCL GOS Institute of Child Health, 30 Guilford Street, London, WC1N 1EH, UK

2 Department of Cell and Developmental Biology, University College London, Gower Street, WC1E 6BT, UK

3 Department of Developmental Neurobiology and MRC Centre for Neurodevelopmental Disorders, IoPPN, Kings College London, New Hunt's House, Guy's Campus, London, SE1 1UL, UK

4 School of Biological and Behavioural Sciences, Faculty of Science and Engineering, Queen Mary University of London, London E1 4NS, UK

5 Cambridge Institute of Therapeutic Immunology & Infectious Disease (CITIID), Jeffrey Cheah Biomedical Centre, University of Cambridge, Puddicombe Way, Cambridge, CB2 0AW

6 Center for Integrative Biology, Facultad de Ciencias, Universidad Mayor, Santiago, Chile

7 Escuela de Biotecnología, Facultad de Ciencias, Universidad Mayor, Santiago, Chile

8 Department of Molecular Life Sciences, University of Zurich, Winterthurerstrasse 190, 8057, Zurich, Switzerland.

Disease Models & Mechanisms • DMM • Accepted manuscript

9 Department of Neuroscience, Physiology & Pharmacology, University College London, Gower Street, WC1E 6BT, UK

10 School of Life Sciences, University of Sussex, Brighton, BN1 9QJ, UK

***Corresponding authors:**

k.tuschl@ucl.ac.uk, https://orcid.org/0000-0001-8599-8516

e.busch-nentwich@qmul.ac.uk, https://orcid.org/0000-0001-6450-744X

Key words: zebrafish, slc39a14, manganese, calcium, transcriptome

Summary statement

Transcriptome analysis of zebrafish *slc39a14*$^{-/-}$ mutants demonstrates that loss of *slc39a14* leads to concurrent manganese neurotoxicity and deficiency, both associated with calcium dyshomeostasis.

Abstract

Manganese neurotoxicity is a hallmark of Hypermanganesemia with Dystonia 2, an inherited manganese transporter defect caused by mutations in SLC39A14. To identify novel potential targets of manganese neurotoxicity we performed transcriptome analysis of *slc39a14*$^{-/-}$ mutant zebrafish unexposed and exposed to $MnCl_2$. Differentially expressed genes mapped to the central nervous system and eye, and pathway analysis suggested that calcium dyshomeostasis and activation of the unfolded protein response are key features of manganese neurotoxicity. Consistent with this interpretation, $MnCl_2$ exposure led to decreased whole animal calcium levels, locomotor defects and changes in neuronal activity

within the telencephalon and optic tectum. In accordance with reduced tectal activity, *slc39a14*$^{-/-}$ zebrafish showed changes in visual phototransduction gene expression, absence of visual background adaptation and a diminished optokinetic reflex. Finally, numerous differentially expressed genes in mutant larvae normalised upon $MnCl_2$ treatment indicating that, in addition to neurotoxicity, manganese deficiency is present either subcellularly or in specific cells or tissues. Overall, we assembled a comprehensive set of genes that mediate manganese-systemic responses and found a highly correlated and modulated network associated with calcium dyshomeostasis and cellular stress.

Introduction

SLC39A14 is a manganese (Mn) uptake transporter essential for the maintenance of Mn homeostasis (Thompson and Wessling-Resnick, 2019). Mutations in SLC39A14 impair cellular Mn uptake and result in systemic Mn overload characterised by hypermanganesemia and neurodegeneration (Tuschl et al., 2016; Juneja et al., 2018; Marti-Sanchez et al., 2018; Rodan et al., 2018; Zeglam et al., 2018). In patients, subsequent accumulation of Mn in the globus pallidus, part of the basal ganglia involved in motor control, leads to rapidly progressive dystonia-parkinsonism with onset in early childhood, a condition known as Hypermanganesemia with Dystonia 2 (HMNDYT2, OMIM 617013). In a small number of patients, treatment has been attempted with Mn chelation using intravenous disodium calcium edetate ($Na_2CaEDTA$) (Tuschl et al., 2016; Rodan et al., 2018; Lee and Shin, 2022) similar to a protocol established for HMNDYT1 (OMIM 613280) which is caused by mutations in SLC30A10, a Mn exporter required for biliary excretion of Mn (Tuschl et al., 1993; Tuschl et al., 2012). Brain magnetic resonance imaging (MRI) appearances of patients with either disorder are indistinguishable with hyperintensity of both the basal ganglia, particularly the globus pallidus, and the white matter on T1-weighted imaging (Tuschl et al., 2012; Tuschl et al., 2016). While patients with HMNDYT1 show significant improvement of

neurological symptoms upon treatment initiation (Tuschl et al., 2008; Tuschl et al., 2012), individuals with HMNDYT2 have variable treatment responses, with some patients experiencing a worsening of their movement disorder (Tuschl et al., 2016; Marti-Sanchez et al., 2018). The reasons for the difference in treatment response are poorly understood.

Although an essential trace metal, excess Mn acts as a neurotoxicant. Environmental Mn overexposure leads to preferential Mn accumulation in the globus pallidus similar to that observed in inherited Mn transporter defects and causes manganism, a Parkinsonian movement disorder characterised by bradykinesia, akinetic rigidity, and dystonia, accompanied by psychiatric disturbances (Blanc, 2018; Chen et al., 2018). Despite the recognised role of Mn in neurodegenerative disease processes the mechanisms related to Mn neurotoxicity remain poorly understood. The clinical similarities between manganism and Parkinson's disease (PD) suggest that dopaminergic signalling is impaired upon Mn toxicity. However, in manganism, dopaminergic neurons within the substantia nigra are intact and response to L-DOPA, mainstay of treatment in PD, is poor (Koller et al., 2004). Glutamatergic excitotoxicity as well as altered gamma-aminobutyric acid (GABA) signalling have also been proposed to underlie Mn-associated neurodegeneration (Caito and Aschner, 2015). Indeed, Mn toxicity is likely mediated by a number of processes including oxidative stress, impaired mitochondrial function, protein misfolding and aggregation, and neuroinflammation (Martinez-Finley et al., 2013; Tjalkens et al., 2017).

We have recently established and characterised a zebrafish loss-of-function mutant *slc39a14*$^{U801/U801}$ (herein referred to as *slc39a14*$^{-/-}$) that closely resembles the human phenotype with systemic accumulation of Mn, particularly in the brain (Tuschl et al., 2016). Homozygous mutants develop increased susceptibility to Mn toxicity and impaired locomotor behaviour upon Mn exposure. Mn levels can be lowered through chelation with $Na_2CaEDTA$ similar to what is observed in human patients (Tuschl et al., 2016).

In this study, we performed RNA sequencing on individual *scl39a14*$^{-/-}$ larvae and their unaffected siblings to identify novel potential targets of Mn toxicity. Furthermore, we determined the transcriptional signature elicited in response to $MnCl_2$ treatment in *scl39a14*$^{-/-}$ and unaffected sibling larvae. Our results provide evidence that, in addition to Mn neurotoxicity, partial Mn deficiency that corrects upon Mn treatment is a prominent feature of *slc39a14* loss-of-function. We determined that Ca^{2+} dyshomeostasis is a likely key event in both Mn deficiency and overload. Mn neurotoxicity is further associated with activation of the unfolded protein response (UPR), oxidative stress, mitochondrial dysfunction, apoptosis and autophagy, and disruption of proteostasis. These changes accompany impaired neuronal activity within the telencephalon and optic tectum, as well as associated behaviours, of *slc39a14*$^{-/-}$ zebrafish.

Results

Transcriptome analysis of *slc39a14*$^{-/-}$ mutants identifies increased sensitivity to Mn toxicity as well as Mn deficiency effects

To investigate the transcriptional profiles of *slc39a14*$^{-/-}$ mutants in the absence and presence of Mn treatment, embryos from a heterozygous incross were split into two groups and either raised under standard conditions (subsequently referred to as unexposed), or treated with 50µM $MnCl_2$ from 2 until 5 days post fertilisation (dpf) (Fig. 1A). We have previously shown that this concentration elicits a pronounced locomotor phenotype in homozygous mutant larvae compared to siblings (Tuschl et al., 2016). We then carried out transcriptional profiling of individual 5 dpf larvae using 3' tag sequencing (differential expression transcript counting technique, DeTCT) (Collins et al., 2015). Principal Component Analysis (PCA) showed an effect of homozygosity and treatment status, but no difference between heterozygous and wild-type individuals (Fig. 1B, Table S1). We therefore pooled the wild-type and heterozygous embryos in the analysis for better statistical confidence and simplicity.

Analysis of differentially expressed genes between the four conditions produced three groups of genes, each with a characteristic expression profile. The first group are genes that were differentially expressed in $MnCl_2$ exposed siblings compared with unexposed siblings and represent a response to an increased concentration of Mn in the embryos (Fig. 1C, Mn toxicity). The second group are genes that show increased sensitivity to Mn in *slc39a14*$^{-/-}$ mutants. These are defined as genes that are differentially expressed in $MnCl_2$ exposed mutants compared with unexposed siblings, but not differentially expressed in unexposed mutants compared to unexposed siblings or exposed siblings compared with unexposed siblings (Fig. 1D, Increased sensitivity). The third group is composed of genes that were differentially expressed in unexposed mutants compared with unexposed siblings (Fig. 1E, Mutant effect). We will now consider these three groups of genes in turn (see Table 1 for examples and Table S2 and S3 for the top 10 up- and downregulated genes and highest p-values from each differentially expressed gene list).

Mn toxicity causes genotype-independent differential gene expression

$MnCl_2$ treatment caused differential expression of 328 genes independent of the genotype (comparing $MnCl_2$ exposed and unexposed siblings) (Fig. 2A, Table 1 and Table S1). Among them is *brain-derived neurotrophic factor* (*bdnf*), a previously reported read-out for Mn exposure (Zou et al., 2014), that also showed diminished expression in untreated mutants compared to siblings (Fig. 2B). BDNF signalling has been linked to the maturation of parvalbumin positive cells, mainly GABAergic interneurons (Fairless et al., 2019). However, parvalbumin encoding genes were more highly expressed upon Mn exposure in mutants (*pvalb1, pvalb2*, *pvalb8*) as well as siblings (*pvalb2*, *pvalb8*).

Among other brain-expressed genes affected by $MnCl_2$ exposure were some involved in synaptic vesicle function (*rims2b*, *stxbp1a, sv2a*, *sypb*, *syt9a*), and genes encoding the Metabotropic Glutamate Receptor (*grm8a*), β-Synuclein (*sncb*) and Ephrin-B Membrane Proteins (*efnb1*, *efnb2a*), all of which had decreased expression (Table 1).

Analysis of annotations to Gene Ontology (GO) terms (Fig. 2C; Table S4; Fig. S1 for GO enrichment split by up- and downregulation) showed enrichments of terms related to lipid metabolism (driven by upregulation of, for example, *apoa4b.2*, *apoa4a*, *apoea*), blood cell development (upregulation of *alas1*, *fech*, *soul5*), translation (35 ribosomal protein encoding genes, most of which were upregulated) and circadian rhythm (upregulation of *cry1aa*, *cry1bb*, *cryba4*, *per3*). These findings are similar to previous reports in which links between Mn toxicity and lipid metabolism (Luo et al., 2020), circadian clock gene regulation (Li et al., 2017), heme-enzyme biogenesis (Chino et al., 2018), and protein biosynthesis (Hernandez et al., 2019) have been described.

Mn is important for connective tissue integrity and bone mineralisation as a constituent of metalloenzymes and enzyme activator (Sirri et al., 2016; Zofkova et al., 2017). Consistent with its role in connective tissues maintenance, transcriptome analysis confirmed that Mn exposure in zebrafish led to reduced expression of multiple connective tissue related genes (*col2a1b*, *col4a5*, *col9a1a*, *col9a2*, *col11a2*, *dcn*, *fbn2b*, *matn1*).

slc39a14$^{-/-}$ mutants show increased sensitivity to $MnCl_2$ treatment

Our analysis showed that 613 genes were differentially expressed in $MnCl_2$ exposed mutants compared with unexposed siblings, with no significant expression changes in either unexposed mutants or exposed siblings. Therefore, these are genes that showed increased sensitivity to $MnCl_2$ exposure in *slc39a14*$^{-/-}$ mutant larvae (Fig. 3A, Table 1). 15% (95/613) of these genes also have a significant genotype-treatment interaction effect meaning that there was a synergistic effect on expression of treating mutant embryos with $MnCl_2$ – that is the combined estimated effects of genotype and $MnCl_2$ treatment alone were significantly less than the estimated log2 fold change for $MnCl_2$ exposed mutants when compared to unexposed siblings (Fig. 3B, see Table S1 for synergistic genes in bold). The remaining genes (518/613) showed expression changes consistent with additive effects of the sub-significance threshold responses to genotype and $MnCl_2$ exposure alone (Fig. 3C). Results

from the transcriptome analysis were validated by qRT-PCR for a subset of six genes (*bdnf*, *gnat2*, *hspa5*, *opn1mw2*, *pde6h*, *prph2b*) using RNA extracted from equivalent embryos in a different experiment (Fig. 3D–E, Fig. S2 and Table S5). Changes in gene expression observed by qRT-PCR for all six genes were consistent with the results obtained from transcript counting (compare Fig. 3B with Fig. 3D and Fig. 3C with Fig. 3E).

Enrichment of zebrafish anatomy (ZFA) terms showed that genes differentially expressed upon $MnCl_2$ exposure in *slc39a14*$^{-/-}$ mutants are disproportionately expressed in the nervous system including the eye (Fig. 3F; Fig. S3; Table S6). This is confirmed by the enrichment of GO terms such as visual perception and phototransduction, associated with genes that were downregulated (Fig. 3G, Fig. S1). Also enriched were terms related to the ribosome, translation and the unfolded protein response (UPR), suggesting effects on protein synthesis and folding (Fig. 3G, Fig. S1 and Table S4).

Increased sensitivity of *slc39a14*$^{-/-}$ mutants to $MnCl_2$ treatment leads to Mn neurotoxicity

Enriched ZFA terms identified in $MnCl_2$ exposed *slc39a14*$^{-/-}$ mutants that were not present in siblings showed a high number of differentially expressed genes in the nervous system (Table S6) confirming the role of raised Mn in neurotoxicity. We found *slc1a2a*, encoding the astrocytic glutamate transporter excitatory amino acid transporter (EAAT2), as the fifth most highly and significantly downregulated gene upon $MnCl_2$ exposure (Table S2 and S3). A role for astrocyte mediated Mn neurotoxicity and neuroinflammation was further suggested by increased expression of the astrocyte related genes *atf5a*, *atf5b* and *gfap*. In addition, expression of the teleost specific glutamate transporters *slc1a2b* (upregulated) and *slc1a8a* (downregulated) was altered pointing towards involvement of the glutamate-glutamine cycle in Mn neurotoxicity. Two genes required for the regulation of ionotropic AMPA type glutamate receptors (*nsg2*, *prrt1*) also showed diminished expression in $MnCl_2$ treated mutants (Table 1).

Furthermore, we observed increased expression of *slc6a11b*, encoding a GABA uptake transporter, as well as the Parvalbumin encoding gene (*pvalb1*) present in GABAergic interneurons. Expression of the GABA-A receptor encoding genes *gabra6a* and *gabrb3*, and *nptxrb*, encoding the Neuronal Pentraxin Receptor expressed in Parvalbumin positive interneurons (Kikuchihara et al., 2015), was reduced.

Despite the assumption that abnormal dopamine signalling is a major player in Mn neurotoxicity (Guilarte and Gonzales, 2015) only two genes linked to Dopamine, *gnb5b* (downregulated) and *gpr37l1b* (upregulated), both of which encode proteins that interact with neurotransmission via the Dopamine D2 Receptor (Octeau et al., 2014; Hertz et al., 2019), were differentially expressed.

In order to assess the effects of Mn neurotoxicity on neuronal function we performed *in situ* hybridization chain reaction to map *gad1b* mRNA in $MnCl_2$ exposed wild-type and mutant siblings. *gad1b* was chosen because Mn preferentially accumulates in the globus pallidus, a region that is particularly rich in GABAergic projections, both in individuals with Mn overexposure and those with inherited Mn transporter defects. However, spatial *gad1b* expression analysis did not suggest changes in GABAergic signalling and brain structure (data not shown).

$MnCl_2$ exposure alters resting-state neuronal activity and locomotor behaviour

cfos is an immediate early gene induced in response to neuronal activity and so we performed *in situ* hybridization chain reaction to map changes in *cfos* expression in response to $MnCl_2$ exposure as a proxy for identifying resting-state changes in neuronal activity. We observed pronounced alterations in *cfos* expression in both $MnCl_2$ treated wild-type and mutant siblings (Fig. 4A-D). Consistent with the increased sensitivity to Mn neurotoxicity suggested by RNA sequencing, homozygous mutant larvae showed more extensive changes in *cfos* expression compared to siblings. Specific enhanced expression, reflecting increased neuronal activity, was particularly evident within the telencephalon in mutant

versus wild-type larvae, while lower expression was observed within the optic tectum of mutants (Fig. 4D).

We next tracked the locomotor behaviour of unexposed and $MnCl_2$ exposed wild-type and mutant larvae from 4 to 7dpf on a 14:10 light dark cycle. Homozygous mutants showed a dose dependent reduction in average locomotor activity during the day and increased locomotor activity during the night while wild-type larvae remained unaffected by $MnCl_2$ exposure (Fig. 5A, Table S7). Wild-type fish sharply increase their locomotor activity immediately following lights OFF and gradually, over several minutes, return to baseline locomotor activity, a behaviour known as the visual motor response (VMR) (Burton et al., 2017). Frame-by-frame analysis of larval locomotion showed that *slc39a14*$^{-/-}$ zebrafish have a preserved VMR but show hyperlocomotion throughout the first hours following lights OFF, with larvae returning to baseline activity only towards the second half of the night (Fig. 5B).

Increased sensitivity of *slc39a14*$^{-/-}$ mutants to $MnCl_2$ treatment is associated with gene expression changes affecting calcium and protein homeostasis, and the unfolded protein response

Mn toxicity is known to cause protein misfolding and aggregation (Angeli et al., 2014; Harischandra et al., 2019b) and, as previously shown for Mn overexposure in *C. elegans* (Angeli et al., 2014), multiple genes involved in the UPR had increased expression in *slc39a14*$^{-/-}$ mutants with *hspa5*, *atf3* and *xbp1* observed as the most highly and significantly upregulated genes upon $MnCl_2$ treatment (Table 1 and Table S2 and S3). This is supported by transcription factor motif enrichment analysis using Hypergeometric Optimization of Motif EnRichment analysis (HOMER) (Heinz et al., 2010), which showed that the dysregulated genes are enriched for Chop/Atf4 binding sites among others (Fig. S3, Table S8). Degradation of misfolded and aggregated proteins occurs via the ubiquitin-proteasome system within the cytosol (Tamas et al., 2014) and $MnCl_2$ exposed *slc39a14*$^{-/-}$ mutants showed gene expression changes linked to ubiquitination (Table 1). Ca^{2+} homeostasis within

the endoplasmic reticulum (ER) plays a major role during the UPR and vice versa (Groenendyk et al., 2021). Potentially linked to the UPR, over a dozen Ca^{2+} associated/dependent genes were differentially expressed in $MnCl_2$ treated *slc39a14*$^{-/-}$ mutants (Table 1, Table S1).

Given the observed changes in expression of Ca^{2+} linked genes, we next assessed total Ca, Mg and Mn levels in both wild-type and mutant larvae by Inductively Coupled Plasma Mass Spectrometry (ICP-MS). Consistent with a disturbance in Ca^{2+} homeostasis, we found that $MnCl_2$ treatment in both wild-type and mutant larvae led to a marked decrease in total Ca and Mg levels (Fig. 5C). As previously observed, Mn accumulation was much greater in mutant larvae (Fig. 5C). These results confirm that Mn overload leads to Ca^{2+} dyshomeostasis associated with expression changes of key genes responsible for Ca^{2+} regulation.

Activation of the UPR as well as Ca^{2+} dyshomeostasis can promote apoptosis and autophagy. Concordantly, genes involved in autophagy and apoptosis were differentially expressed (Table 1). In particular, *faim2b*, which encodes the recently identified novel regulator of autophagy FAIM2B (Hong et al., 2020), was the third most highly upregulated gene in $MnCl_2$ exposed *slc39a14*$^{-/-}$ mutants (Table S2). Also, the expression of *ubcn*, encoding a beclin 1 interactor and responsible for autophagy initiation (Liu et al., 2019), was increased upon $MnCl_2$ exposure.

To further explore whether increased apoptotic cell death may be responsible for the high number of downregulated genes observed upon $MnCl_2$ exposure, we performed Terminal deoxynucleotidyl transferase dUTP Nick End Labelling (TUNEL) staining on brains from unexposed and $MnCl_2$ exposed wild-type and mutant larvae (Fig. 5D). However, there was no difference in the number of TUNEL positive cells between unexposed and $MnCl_2$ exposed larvae of either genotype suggesting that functional rather than neurodegenerative changes are responsible for Mn neurotoxicity effects.

Oxidative stress and mitochondrial dysfunction are prominent features of Mn toxicity (Smith et al., 2017; Harischandra et al., 2019a). Consistent with this observation, essential genes of the thioredoxin/peroxiredoxin system (*prdx1*, *txn*, *txnrd3*) were activated in $MnCl_2$ exposed *slc39a14*$^{-/-}$ mutants. Likewise, genes related to mitochondrial function showed differential expression in $MnCl_2$ treated mutants (Table 1). Our data therefore further supports a role of mitochondrial impairment in Mn induced neurotoxicity.

Increased sensitivity of *slc39a14*$^{-/-}$ mutants to $MnCl_2$ causes visual impairment

Consistent with the reduced *cfos* expression/neuronal activity observed within the optic tectum (Fig. 4), 30 genes involved in phototransduction were differentially expressed (27/30 genes were reduced) in $MnCl_2$ exposed mutants but not in siblings (Fig. 6A, Table S1). These included some of the most significantly upregulated genes such as *pde6ha*, *opn1mw2*, *opn1mw1* and *rcvrna* in the increased sensitivity group (Table S2 and S3). Hence, we further examined the vision of *slc39a14*$^{-/-}$ mutants. In zebrafish, visual background adaptation (VBA), the ability to aggregate and disperse melanosomes to in order to adapt their body pigmentation to the environment, requires retinal input and is impaired in blind larvae (Mueller and Neuhauss, 2014).

We observed that $MnCl_2$ exposed *slc39a14*$^{-/-}$ mutant larvae lacked melanosome aggregation and remained dark following light exposure from 4dpf while exposed wild-type larvae and unexposed mutants demonstrated a normal VBA (Fig. 6B). Next, we analysed the optokinetic response (OKR) in homozygous *slc39a14*$^{-/-}$ larvae at 5 dpf after $MnCl_2$ exposure. Exposed mutant larvae demonstrated a significant reduction in slow phase eye velocity at high spatial frequencies suggesting impaired visual acuity (Fig. 6C, Table S9). Retinal histology of mutant and $MnCl_2$ exposed animals appeared normal, suggesting functional rather than overt structural deficits (Fig. 6D). In conclusion, the reduced expression of phototransduction genes in combination with reduced *cfos* expression/neuronal activity

within the optic tectum, impaired VBA and OKR as well as abnormal VMR reveal that Mn exposure in *slc39a14*$^{-/-}$ larvae leads to visual impairment.

Most differentially expressed genes in unexposed *slc39a14*$^{-/-}$ mutants are rescued by Mn treatment suggesting Mn deficiency

When compared to unexposed siblings, 266 genes showed significantly different expression due to homozygous state alone (unexposed homozygous mutants versus unexposed unaffected siblings) (Fig. 7A; Table S1). Expression of 12% of these genes (31/266) was also significantly different between $MnCl_2$ exposed mutants and unexposed siblings (Fig. 7B). Seven of these genes overlap with those differentially expressed in siblings upon $MnCl_2$ exposure, suggesting that these genes were the most sensitive targets of Mn toxicity (*alas1*, *atp2a1*, *bdnf*, *crim1*, *dio3b*, *dip2ca*, *rims2b*). However, the majority (88%, 235/266) of differentially expressed genes in unexposed mutants are not significantly differentially expressed when comparing $MnCl_2$ exposed mutants and unexposed siblings (Fig. 7C). This suggests that the homozygous *U801* mutation creates Mn deficiency leading to gene expression changes that return to levels observed in unexposed unaffected siblings upon $MnCl_2$ treatment.

Analysis of ZFA terms within this rescued set of genes demonstrated enrichment of terms related to the nervous system (Fig. 7D; Figure S3; Table S6). For instance, brain expressed genes that showed reduced expression upon Mn deficiency include some essential for synaptic function and vesicle formation (*snap25a*, *sv2a*, *sypb*, *syt6a*, *syt9a*), neurite and axonal growth (*dock3*, *gas7a*, *kalrna*, *kalrnb*, *lrrc4c*) and potassium channels (*kcnc1a*, *kcnc3a*). GO term analysis linked differential gene expression to cell-cell adhesion and cell-cell interactions (Fig. 7E; Figure S1; Table S4). Expression of seven protocadherin encoding genes was altered with *pcdh7b* as the third most highly downregulated gene within this group. Protocadherins are Ca^{2+} dependent cell adhesion proteins primarily expressed in the brain where they regulate synapse maturation, function and plasticity (Mancini et al., 2020).

In addition, several other Ca^{2+} associated genes were returned to normal expression levels by Mn treatment distinct from those changed due to Mn toxicity. These included genes encoding Ca^{2+} ATPases (*atp2a1*, *atp2b3b*), Ca^{2+} channels (*cacnb4b*), Ca^{2+} activated potassium channels (*kcnma1a*, *kcnn1a*), calmodulins (*calm1b*, *calm3a*) and calmodulin binding proteins (*camta1b*, *strn4*). These results suggest that in addition to causing a systemic increase in Mn levels, the loss of *slc39a14* function may also result in local Mn deficiency with gene expression changes that can be rescued with exogenous Mn. Differentially expressed genes in both the Mn sensitivity and Mn rescue group link to Ca^{2+} regulation suggesting that disturbed Mn homeostasis has significant consequences on Ca^{2+} dependent genes with a distinct affected gene set for each group (Table1).

Discussion

Transcriptional profiling of *slc39a14* mutant zebrafish has identified distinct gene groups that are differentially expressed in physiological conditions and upon $MnCl_2$ exposure. Consistent with the neurodegenerative phenotype observed in HMNDYT2 patients and the previously described accumulation of Mn in the brain of *slc39a14*$^{-/-}$ zebrafish mutants (Tuschl et al., 2016), the majority of differentially expressed genes map to the CNS and the eye. Mn treatment leads to gene expression changes in both *slc39a14*$^{-/-}$ mutant and sibling zebrafish. However, a much greater number of genes change in mutant larvae upon $MnCl_2$ treatment than in treated non-mutant siblings confirming an increased sensitivity to Mn toxicity that is consistent with previous observations (Tuschl et al., 2016). This is corroborated by the changes in brain activity, locomotor and visual behaviour observed in mutant larvae. Intriguingly, 88% (235/266) of differentially expressed genes in unexposed *slc39a14*$^{-/-}$ mutants normalised upon $MnCl_2$ treatment. This suggests that Mn treatment in *slc39a14*$^{-/-}$ mutants rescues some of the transcriptomic changes observed in unexposed mutants and implies that SLC39A14 loss leads to Mn deficiency in parallel to the observed Mn accumulation.

Unexposed *slc39a14*$^{-/-}$ mutants as well as $MnCl_2$ treated mutants and siblings show evidence of Mn neurotoxicity

The mechanisms underlying Mn neurotoxicity are heterogenous suggesting extensive roles for Mn in brain pathobiology (Soares et al., 2020). The neuronal subtypes affected by Mn neurotoxicity remain the subject of debate. In agreement with previous reports we observed altered expression of genes involved in glutamatergic and GABAergic neurotransmission in $MnCl_2$ treated *slc39a14*$^{-/-}$ mutants (Marreilha Dos Santos et al., 2017). The most highly and significantly downregulated genes included *slc1a2a* encoding the astrocytic glutamate reuptake transporter EAAT2. Transcriptional repression of *SLC1A2* with subsequent impaired glutamate uptake and excitotoxicity has been observed in $MnCl_2$ exposed human astrocytes (Rizor et al., 2021) suggesting that Mn neurotoxicity affects the glutamate-glutamine cycle.

In humans, Mn preferentially accumulates in the globus pallidus, a region that is particularly rich in GABAergic neurons (Sidoryk-Wegrzynowicz and Aschner, 2013; Tuschl et al., 2016). In $MnCl_2$ treated *slc39a14*$^{-/-}$ zebrafish, the expression of genes encoding the GABA-A receptor (*gabra6a, gabrb3*) and the GABA reuptake transporter (*slc6a11b*) was reduced, similar to studies in rats where Mn exposure leads to diminished GABA-A receptor mRNA expression and interferes with GABA uptake in astrocytes (Fordahl and Erikson, 2014; Ou et al., 2017). Increased expression of genes encoding Parvalbumin (*pvalb1, pbalb2* and *pvalb8*) in *slc39a14*$^{-/-}$ mutants and siblings upon $MnCl_2$ treatment may further indicate that GABAergic interneurons are a target of Mn neurotoxicity (Kikuchihara et al., 2015). Parvalbumin, a Ca^{2+} binding protein, can also bind Mn^{2+} with high affinity (Nara et al., 1994). Mn may therefore interact with parvalbumin directly or via changes in Ca^{2+} homeostasis that are clearly evident in *slc39a14*$^{-/-}$ zebrafish. Despite the observed gene expression changes related to GABAergic neurotransmission the spatial localisation of *gad1b* mRNA expression was unchanged in both $MnCl_2$ exposed wild-type and *slc39a14*$^{-/-}$ larvae. However, the observed marked alterations in *cfos* expression suggested altered neuronal activity in

slc39a14$^{-/-}$ compared to with wild-type fish. Enhanced expression/activity was evident within preoptic, hypothalamic, pallidal and subpallidal regions.

Because manganism resembles Parkinson's disease to some extent (e.g. both cause an akinetic movement disorder, albeit with distinct clinical features) it has long been hypothesized that dopaminergic neurons are affected by Mn neurotoxicity (Ijomone et al., 2016). However, transcriptome analysis of *slc39a14*$^{-/-}$ mutants provides little evidence that Mn neurotoxicity causes primary gene expression changes related to dopaminergic signalling.

Consistent with predominant accumulation of Mn in astrocytes rather than neurons (Tjalkens et al., 2017; Gorojod et al., 2018; Popichak et al., 2018), Mn exposure in *slc39a14*$^{-/-}$ mutants leads to increased expression of the astrocyte related genes *atf5a*, *atf5b* and *gfap* as well as the astrocyte expressed glutamate and GABA uptake transporter genes *slc1a2* and *slc6a11b* corroborating a role for glia in Mn neurotoxicity.

Although we observe gene expression changes linked to apoptosis, TUNEL staining did not reveal increased apoptotic cell death upon $MnCl_2$ exposure. This may suggest that Mn neurotoxicity initially and primarily causes deficits in neuronal function rather than neurodegeneration which is in keeping with clinical observations that the neuronal phenotype of affected individuals is to some extent reversible (Tuschl et al., 2016).

Mn toxicity in *slc39a14*$^{-/-}$ mutants is associated with calcium dyshomeostasis, activation of the unfolded protein response and oxidative stress

Our results clearly indicate that Mn imbalance interferes with calcium homeostasis and causes expression changes of calcium associated genes coupled with altered total calcium levels. It is understood that Mn^{2+} can replace Ca^{2+} in its biologically active sites (Kalbitzer et al., 1978; Song et al., 2017) and disrupt Ca^{2+} homeostasis at the mitochondria and the ER, thereby affecting intracellular Ca^{2+} concentrations (Quintanar et al., 2012). Mn overexposure

has previously been shown to disrupt neurotransmitter release via interaction with the SNARE complex and subsequent activation of Calpain, a Ca^{2+}/Mn^{2+}-activated neutral protease (Wang et al., 2018). $MnCl_2$ treatment in *slc39a14*$^{-/-}$ mutants indeed affects expression of genes encoding parts of the presynaptic neurotransmitter release machinery suggesting that Mn neurotoxicity may be mediated through impaired presynaptic exocytosis. Whether this is facilitated via direct interaction of Mn with neurotransmitter release or via Ca^{2+} dysregulation needs to be determined in future studies. Nevertheless, our results provide evidence that Ca^{2+} dysregulation is a key feature of Mn neurotoxicity. This has also been shown for other neurodegenerative disorders including Parkinson's, Alzheimer's and Huntington's disease in which Ca^{2+} dyshomeostasis occurs upstream of protein aggregation (Jadiya et al., 2021).

Ca^{2+} homeostasis is maintained by the ER, the key organelle for regulating proteostasis (Wang et al., 2012). Ca^{2+} dysregulation is closely linked to the UPR and ER stress that is evident in $MnCl_2$ exposed *slc39a14*$^{-/-}$ mutants with upregulation of multiple UPR associated genes. HOMER analysis also confirms enrichment of the Chop/Atf4 motif in $MnCl_2$ treated mutants. This is consistent with previous studies that show increased expression of ATF6 and HSPA5 as well as increased Xbp1 mRNA splicing in Mn exposed brain slices (Xu et al., 2013).

In addition to Ca^{2+} dyshomeostasis, oxidative stress and mitochondrial dysfunction are shared characteristics among neurodegenerative disorders and metal toxicity (Harischandra et al., 2019a). Mn accumulates in mitochondria where it leads to the generation of reactive oxygen species (ROS) (Rizor et al., 2021). ROS production can further exacerbate protein misfolding (Nakamura et al., 2021). Oxidative stress is highlighted in $MnCl_2$ exposed *slc39a14*$^{-/-}$ mutants by the upregulation of the thioredoxin/thioredoxin reductase and peroxiredoxin system, similar to previous results in rats (Taka et al., 2012). ROS also cause apoptosis and autophagy via lysosomal membrane permeabilisation and cathepsin release (Gorojod et al., 2017; Wang et al., 2017; Porte Alcon et al., 2018; Zhi et al., 2019; Tinkov et

al., 2021). In accordance, we observe changes in autophagy and cathepsin gene expression upon $MnCl_2$ treatment in mutant larvae, however, we did not see alterations in the number of apoptotic cells determined by TUNEL staining.

In summary, transcriptome analysis of *slc39a14*$^{-/-}$ zebrafish suggests that Mn overexposure affects a multitude of molecular processes. The future challenge will be the identification of the trigger event that leads to Mn induced calcium dyshomeostasis as well as mitochondrial and lysosomal dysfunction, a prerequisite for finding novel therapeutic targets for the treatment of Mn neurotoxicity.

Mn toxicity in *slc39a14*$^{-/-}$ zebrafish causes impairments in retinal function

Transcriptome analysis revealed an unsuspected Mn toxicity effect in *slc39a14*$^{-/-}$ zebrafish with more than thirty retinal phototransduction genes differentially expressed. Expression changes were accompanied by impaired VBA and an altered OKR. Combined with the reduced neuronal activity observed within the optic tectum this suggests that Mn has toxic effects on the function of the zebrafish retina. While this has not been observed in affected patients or rodent models of Mn overload, both Mn uptake transporters, SLC39A8 and SLC39A14, are highly expressed in the retinal pigment epithelium (Leung et al., 2008). Furthermore, Mn plays an essential role in retinal function where it is required for normal ultrastructure of the retina (Gong and Amemiya, 1996). Possible differences between the human and zebrafish phenotype may simply be caused by the direct contact of the zebrafish eye with Mn in the water contributing to enhanced ocular Mn uptake and toxicity. We cannot exclude a direct effect of Mn on the oculomotor system and melanophore function leading to the changes in the OKR and VBA observed but the large number of differentially expressed phototransduction genes as well as reduced tectal neuronal activity make Mn induced retinal dysfunction more likely. It is plausible that Mn also affects non-retinal photoreceptors which may link to the expression changes observed for several circadian clock genes as well as the altered VMR. Mn administration in rats has previously been shown to cause

dysregulation of circadian clock gene expressions (Li et al., 2017). Locomotor behavioural analysis of *slc39a14*$^{-/-}$ zebrafish did indeed reveal changes in the locomotor activity pattern with decreased activity during the day and increased activity during the night as well as an altered VMR at light:dark transitions, a behaviour linked to the function of non-visual photoreceptors (Fernandes et al., 2012).

Loss of *slc39a14* function in zebrafish causes Mn deficiency

Perhaps the most intriguing observation was that most differentially expressed genes (235/266) in unexposed *slc39a14*$^{-/-}$ mutants normalised upon $MnCl_2$ treatment. This indicates that whilst SLC39A14 deficiency leads to systemic Mn accumulation it also causes deficiency of Mn in parts of the cell or specific types of cells due to its role as a Mn uptake transporter. This partial Mn deficiency may explain why chelation therapy in patients with HMNDYT2 is less effective compared to those with HMNDYT1, with some patients deteriorating upon Mn chelation (Tuschl et al., 2016; Marti-Sanchez et al., 2018; Rodan et al., 2018).

Mn deficiency in *slc39a14*$^{-/-}$ mutants suggests that some features of HMNDYT2 may overlap with those observed in SLC39A8 deficiency, an inherited Mn transporter defect leading to systemic Mn deficiency (OMIM #616721). Affected individuals present with intellectual disability, developmental delay, hypotonia, epilepsy, strabismus, cerebellar atrophy and short stature (Boycott et al., 2015; Park et al., 2015). However, HMNDYT2 does not share these features aside from cerebellar atrophy described in some patients.

As for Mn toxicity, the majority of “rescued” genes map to the CNS. Several differentially expressed genes link to Ca^{2+} homeostasis and binding, however, these are different to those identified upon Mn overload. Notably, expression of protocadherins and formin related genes is reduced in unexposed *slc39a14*$^{-/-}$ mutants. Protocadherins are mainly expressed in the CNS where they are required for normal neural circuitry activity and regulate synaptic function (Kim et al., 2011). Loss of protocadherin function in mice has been previously

associated with neurodegeneration (Hasegawa et al., 2016). Formins are required for stabilisation of E-cadherins (Rao and Zaidel-Bar, 2016) which may link the changes observed in (proto-) cadherin expression with that of formin-associated genes.

How partial Mn deficiency arises within the brain of *slc39a14*$^{-/-}$ zebrafish remains to be determined. It may stem from differences in the expression patterns of various metal transporters. In the future, single cell RNA sequencing, spatial transcriptomics and proteomics may allow us to distinguish neurons/glial cells affected by Mn neurotoxicity from those with deficiency. Identifying the overlap between chelator-treated and mutant larvae as well as analysis of slc39a14-deficient neuronal cultures will aid to delineate the molecular events underlying partial Mn deficiency in *slc39a14*$^{-/-}$ mutants.

In conclusion, our results demonstrate that partial Mn deficiency may be an additional feature to Mn neurotoxicity in *slc39a14*$^{-/-}$ zebrafish. Overall, the *slc39a14*^{U801} loss-of-function zebrafish mutant are proving an excellent disease model to study the disease pathogenesis of HMNDYT2 as well as Mn neurotoxicity per se.

Materials and Methods

Zebrafish husbandry

Zebrafish were reared on a 14/10h light/dark cycle at 28.5°C at the UCL Zebrafish Facility. Embryos were obtained by natural spawning and staging was performed according to standard criteria (Kimmel et al., 1995). Previously generated *slc39a14*^{U801} loss-of-function zebrafish and their siblings were used for all experiments (Tuschl et al., 2016). Ethical approval for zebrafish experiments was obtained from the Home Office UK under the Animal Scientific Procedures Act 1986.

Preparation of larvae for RNA and DNA extraction

The progeny of a single incross of *slc39a14*$^{U801/+}$ fish were raised in 10-cm Petri dishes filled with fish water (0.3 g/L Instant Ocean, 50 embryos per dish) at 28°C. At 2 dpf, half of the larvae were exposed to $MnCl_2$ added to the fish water at a concentration of 50µM (stock solution 1M $MnCl_2$ made up in water). After 72 hours of exposure (at 5 dpf) single larvae were collected in the wells of a 96 well plate, immediately frozen on dry ice and stored at -80°C. For sequencing, frozen embryos were lysed in 100µl RLT buffer (Qiagen) containing 1µl of 14.3M beta mercaptoethanol (Sigma). The lysate was allowed to bind to 1.8 volumes of Agencourt RNAClean XP (Beckman Coulter) beads for 10 mins. The plate was then applied to a plate magnet (Invitrogen) until the solution cleared and the supernatant was removed without disturbing the beads. While still on the magnet the beads were washed three times with 70% ethanol and total nucleic acid was eluted from the beads as per the manufacturer's instructions. Nucleic acid samples were used for genotyping of individual larvae by KASP assay (LGC Genomics) according to the manufacturer's instructions and the following primers: wild-type allele 5' GGCACATAATAATCCTCCATGGG 3', mutant allele 5' GGGCACATAATAATCCTCCATGGT 3' and common primer 5' CCCTGTATGTAGGCCTTCGGGTT 3'. After DNase treatment, RNA was quantified using either Qubit RNA HS assay or Quant-iT RNA assay (Invitrogen).

Transcript counting

DeTCT libraries were generated as described previously (Collins et al., 2015). Briefly, 300ng of RNA from each genotyped sample was fragmented and bound to streptavidin beads. The 3' ends of the fragmented RNA were pulled down using a biotinylated polyT primer. An RNA oligo containing the partial Illumina adapter 2 was ligated to the 5' end of the bound fragment. The RNA fragment was eluted and reverse transcribed using an anchored oligo dT reverse transcriptase primer containing one of the 96 unique index sequences and part of the Illumina adapter 1. The Illumina adapters were completed during a library amplification

step and the libraries were quantified using either the BioPhotometer (Eppendorf) or Pherastar (BMG Labtech). This was followed by size selection for an insert size of 70–270 bases. Equal quantities of libraries for each experiment were pooled, quantified by qPCR, and sequenced on either HiSeq 2000 or HiSeq 2500.

Sequencing data were analysed as described previously (Collins et al., 2015). Briefly, sequencing reads were processed with the DeTCT detag_fastq.pl (https://github.com/iansealy/DETCT) script and aligned to the GRCz11 zebrafish reference genome with BWA 0.5.10 (Li and Durbin, 2009). The resulting BAM files were processed using the DeTCT pipeline, which results in a list of regions (for simplicity referred to as genes in the Results) representing 3' ends, together with a count for each sample. These counts were used for differential expression analysis with DESeq2 (Love et al., 2014). Each region was associated with Ensembl 95 (Yates et al., 2020) gene annotation based on the nearest transcript in the appropriate orientation. False positive 3' ends, representing, for example, polyA-rich regions of the genome, were filtered using the DeTCT filter_output.pl script with the --strict option. Gene sets were analysed using the Cytoscape plugin ClueGO (Bindea et al., 2009) for gene ontology (GO) enrichment and Ontologizer (Bauer et al., 2008) for Zebrafish Anatomy Ontology (ZFA) enrichment.

Quantitative real time PCR (qRT-PCR)

RNA extraction from 30 zebrafish larvae from the same genotype (homozygous mutant or wild-type) was performed using 500µL TRIzol reagent (Invitrogen) according to the manufacturer's protocol and purified using the RNeasy MiniKit (Qiagen). cDNA was generated using GoScript Reverse Transcriptase (Promega). qRT-PCR was performed using GoTaq qPCR Master Mix (Promega) according to the recommended protocol. All samples were run in triplicates. qRT-PCR was carried out on a CFX96 Touch Real-Time PCR Detection System (BioRad). Only primer pairs with R2 values >0.99 and amplification efficiencies between 95% and 105% were used. Relative quantification of gene expression

was determined using the $2^{-\Delta\Delta Ct}$ method, with elongation factor 1α (*ef1α*) as a reference gene (Livak and Schmittgen, 2001). The following primer sequences were used: *ef1α* forward 5' GTACTTCTCAGGCTGACTGTG 3', reverse 5' ACGATCAGCTGTTTCACTCC 3'; *bdnf* forward 5' AGATCGGCTGGCGGTTTATA 3', reverse 5' CATTGTGTACACTATCTGCCCC 3'; *gnat2* forward 5' GCTGGCAGACGTCATCAAAA 3', reverse 5' CTCGGTGGGAAGGTAGTCAG 3'; *hspa5* forward 5' GCTGGGCTGAATGTCATGAG 3', reverse 5' CAGCAGAGACACGTCAAAGG 3'; *opn1mw2* forward 5' GCTGTCATTTCTGCGTTCCT 3', reverse 5' GACCATGCGTGTTACTTCCC 3'; *pde6h* forward 5' CTCGCACCTTCAAGAGCAAG 3', reverse 5' CATGTCTCCAAACGCTTCCC 3'; *prph2b* forward 5' GCCCTGGTGTCCTACTATGG 3', reverse 5' CTCTCGGGATTCTCTGGGTC 3'.

ICP-MS analysis of metal ions

ICP-MS analysis of zebrafish larvae was performed as previously described (Tuschl et al., 2016). In brief, 10 larvae of the same genotype, anaesthetized with MS-222 (4% Tricaine), were pooled and washed several times with distilled H_2O. Samples were digested in 200µl concentrated nitric acid at 95°C until dry and resuspended in 1mL 3% nitric acid. Further dilution with 20% nitric acid to a final volume of 2mL was done prior to analysis. Metals (^{24}Mg, ^{44}Ca and ^{55}Mn) were measured using an Agilent 7500ce ICP-MS instrument with collision cell (in He mode) and Integrated Autosampler (I-AS) using ^{72}Ge as internal standard. The following experimental parameters were used : a) plasma: RF power 1500 W, sampling depth 8.5mm, carrier gas 0.8L/min, make-up gas 0.11 L/min; b) quadrupole: mass range 1-250 amu, dwell time 100 msec, replicates 3, integration time 0.1sec/point. Calibration solutions were prepared for each element between 0 and 200ng/mL using certified reference standards (Fisher Scientific, UK).

Apoptosis analysis

The TUNEL (Terminal deoxynucleotidyl transferase dUTP Nick End Labelling) assay was used to determine apoptotic cell death. Larvae were fixed at 5dpf overnight at 4°C in 4% paraformaldehyde (PFA) and 4% sucrose. Brains were manually dissected, transferred to methanol and stored at -20°C. After rehydration in PBSTr (PBS with 0.5% Triton X-100) brains were permeabilised using 1x proteinase K for 15 minutes. Following washes in PBSTr, the samples were incubated at -20°C in pre-chilled ethanol:acetone (2:1) for 10 min followed by washes in PBSTr. After 1 hour incubation in Apoptag equilibration buffer (Millipore) the samples were incubated in 35µL of TdT enzyme mix (24µL reaction buffer, 12µL TdT enzyme [both Millipore], 1µL 10% Triton-X100) at 37°C overnight. Following washes in PBSTr and incubation in blocking solution (for 1 mL: 100µl normal goat serum, 10µL of DMSO, 0.89 mL PBSTr) for two hours at room temperature, the samples were incubated with polyclonal anti-Digoxigenin-AP antibody (Roche) at a concentration of 1:2000 in blocking solution at 4°C overnight and the samples developed using 4-nitro blue tetrazolium chloride and 5-bromo-4-chloro-3-indolyl-phosphate, toluidine-salt (Roche). Imaging was performed in 80% methanol on a Nikon Eclipse E1000 microscope using the Openlab 4.0.2 software package.

Whole mount *in situ* hybridization chain reaction (HCR)

Larvae were fixed in PFA with 4% sucrose overnight at 4°C, transferred into PBS the next morning and the brain dissected by removing skin, cartilage, and eyes with forceps. For each target mRNA, custom DNA probe sets were designed and ssDNA oligos ordered from Life Technologies, ThermoFisher. DNA HCR amplifiers (comprising a pair of fluorophore-labeled DNA hairpins for Alexa 488 and Alexa 568), and hybridization, wash and amplification buffers was purchased from Molecular Instruments (molecularinstruments.org). *in situ* HCR was performed using a published protocol (https://files.molecularinstruments.com/MI-Protocol-HCRv3-Zebrafish-Rev7.pdf) (Choi et al., 2018). For probe sets and

amplifier details for each target mRNA (*cfos* and *gad1b*) see Table S10. Imaging was performed on a Zeiss Z1 Lightsheet microscope with a 10x imaging objective. Whole-brain image stacks were registered to a *gad1b* reference brain aligned to Zebrafish Brain Browser (Marquart et al., 2015) co-ordinates using Advanced Normalization Tools (ANTs) as reported in (Marquart et al., 2017).

Following registration, we applied image analysis using ImageJ, MATLAB and custom-written scripts in Python. We first applied a 3D median filter to the image stacks and subsequently performed permutation testing to detect changes in cfos signal between two groups as described in (Randlett et al., 2015). This resulted in image stacks with cfos pixels that were enhanced or suppressed between control and treatment groups. These image stacks were then processed to determine their distribution across 168 different anatomical regions. Publicly available masks for these anatomical regions were used (Gupta et al., 2018). We used a False Discovery Rate (FDR) threshold of 0.05%, resulting in a 99.5% significance threshold for each active voxel. Python script for active voxel calculation in each brain mask and the ANTs script for registration can be found on Figshare: https://dx.doi.org/10.6084/m9.figshare.19550998 and https://dx.doi.org/10.6084/m9.figshare.19551007.

Locomotor behavioural analysis

The behavioural assay was conducted as described previously (Tuschl et al., 2016). In brief, zebrafish embryos and larvae were raised on a 14:10-h light/dark cycle at 28°C. Single larvae were transferred to each well of a flat-bottom, clear polystyrene 96-square-well plate (Whatman) in fish water (650 µL) at 4 dpf. Mn exposure was achieved by adding $MnCl_2$ directly to the fish water at the desired concentration (stock solution of 1M $MnCl_2$ made in distilled water). The 96-well plate was maintained at a constant temperature (28.5 C) and exposed to a 14:10-h white light/dark schedule with constant infrared illumination within a custom-modified Zebrabox (Viewpoint Life Sciences). The locomotor behaviour of zebrafish

larvae was tracked from 4 to 7 dpf using an automated video tracking system (Viewpoint Life Sciences). Larval movement was recorded using Videotrack Quantization mode. The Videotrack detection parameters were empirically defined for clean detection of larval movement with minimal noise. A custom-designed MATLAB code was used to extract the average activity data of each larva as described previously (Rihel et al., 2010). Frame-by-frame analysis (25 frames per second) was performed as described by Ghosh and Rihel using the published MATLAB code (Ghosh and Rihel, 2020).

Optokinetic response (OKR)

The OKR was examined using a custom-built rig to track horizontal eye movements in response to whole-field motion stimuli. Larvae at 4 dpf were immobilised in 1.5% agarose in a 35 mm petri dish and analysed at 5 dpf. The agarose surrounding the eyes was removed to allow normal eye movements. Sinusoidal gratings with spatial frequencies of 0.05, 0.1, 0.13 and 0.16 cycles/degree were presented on a cylindrical diffusive screen 25 mm from the centre of the fish's head. Gratings had a constant velocity of 10 degrees/second and changed direction and/or spatial frequency every 20 seconds. Eye movements were tracked under infrared illumination (720 nm) at 60 Hz using a Flea3 USB machine vision camera and custom-written software. A custom-designed Matlab code was used to determine the eye velocity in degrees per second (available at https://bitbucket.org/biancolab/okrsuite).

Retinal histology

5dpf larvae were fixed in 4% PFA overnight at 4°C. Dehydration was achieved by a series of increasing ethanol concentrations in PBS (50%, 70%, 80%, 90%, 95% and 100% ethanol). After dehydration larvae were incubated in a 1:1 ethanol Technovit 7100 solution (1% Hardener 1 in Technovit 7100 basic solution) for 1 h followed by incubation in 100% Technovit solution overnight at room temperature (Heraeus Kulzer, Germany). Larvae were

than embedded in plastic moulds in Technovit 7100 polymerization medium and dried at 37°C for 1 h. Sections of 3 µm thickness were prepared with a microtome, mounted onto glass slides, and dried at 60°C. Sections were stained with Richardson (Romeis) solution (0.5% Borax, 0.5% Azur II, 0.5% Methylene Blue) and slides were mounted with Entellan (Merck, Darmstadt, Germany). Images were taken in the brightfield mode of a BX61 microscope (Olympus).

Experimental design and statistical analyses

Animals were divided into four experimental groups: unexposed homozygous *slc39a14*$^{-/-}$ mutants and their siblings (wild-type and heterozygous genotypes), and $MnCl_2$ exposed homozygous *slc39a14*$^{-/-}$ mutants and their siblings (wild-type and heterozygous genotypes). For the DeTCT data, an equal number of wild-type and heterozygous embryos were selected (see Fig. 1 for numbers of embryos for each experimental group). This was to investigate the possibility of transcriptional changes in the heterozygous embryos compared with wild-type ones. This is not the case; the PCA shows that heterozygous embryos group with wild-type embryos and not separately. Differential expression analysis returns only 11 genes that are statistically different between untreated heterozygotes and untreated wild-types (4 of these genes are on the same chromosome as *slc39a14* and likely represent the effect of allele-specific expression linked to the mutation). There are only 20 genes that are differentially expressed between Mn-exposed heterozygotes and Mn-exposed wild-type embryos with three being linked to *slc39a14*. These lists have been included in S1 Table for completeness. Because of the lack of effect, wild-type and heterozygous embryos were pooled as unaffected siblings for the remaining analysis.

Embryos were all derived from a single cross to minimise the amount of biological variance not caused by the experimental conditions (i.e. genotype and Mn exposure). One wild-type Mn-exposed embryo was excluded from the data after visual inspection of the Principal Component Analysis as it did not group with any of the other samples. DESeq2 was used for

differential expression analysis with the following model: ~ genotype + treatment + genotype:treatment. This models the observed counts as a function of the genotype (homozygous vs siblings) and the treatment (Mn exposed vs unexposed) and an interaction between the two and tests for significant parameters using the Wald test with an adjusted p value (Benjamini-Hochberg) threshold of 0.05.

The 3 groups of differentially expressed genes were defined as follows: 1. Mn toxicity: significant in Mn-exposed siblings vs unexposed siblings; 2. Increased sensitivity: significant in Mn-exposed mutants vs unexposed siblings AND NOT significant in unexposed mutants vs unexposed siblings AND NOT significant in Mn-exposed siblings vs unexposed siblings; 3. mutant effect: significant in unexposed mutants vs unexposed siblings. These groups are not mutually exclusive and some genes appear in more than one group because of the way the groups were defined.

For qRT-PCR, metal and behavioural locomotor analysis, ANOVA with Tukey post-hoc testing and for OKR analysis the Student's t-test was used to determine statistical significance, using the GraphPad Prism software (version 5). For GO term analysis, the settings for ClueGO were as follows: a right-sided hypergeometric test (enrichment only) was used with the Bonferroni step-down (Holm-Bonferroni) correction for multiple testing and terms with corrected p values >0.05 were discarded. For ZFA enrichment analysis, the Ontologizer Parent-Child-Union calculation method was used with Bonferroni correction.

Transcription factor motif analysis

Transcription factor motif enrichment was performed using HOMER's findMotifs.pl tool (v4.10.3) with default settings (Heinz et al., 2010). The GRCz11 promoter set used was created with HOMER's updatePromoters.pl tool based on RefSeq genes from -2000 bp to 2000 bp relative to the transcription start site.

Data Availability Statement:

Sequence data can be downloaded from the European Nucleotide Archive (ENA) using the links provided in Table S11. Supplementary tables are available at Figshare (DOIs specified in the Supplementary Information). The processed count data are available at Figshare (https://doi.org/10.6084/m9.figshare.11808789). All other data are contained within the manuscript and its Supplementary Information files.

Acknowledgments:

We thank the members of the Wilson, Rihel and Bianco labs and other zebrafish groups at University College London (UCL) for helpful discussions. We are grateful to Neha Wali and the Sanger Institute sequencing pipelines for sample processing and sequencing. We thank all supporting staff at UCL including Fish Facility staff for fish care and husbandry.

Financial Disclosure Statement:

K.T. was supported by Action Medical Research (GN1999), the Academy of Medical Sciences, the National Institute for Health Research (NIHR, Academic Clinical Lectureship), the Great Ormond Street Hospital Charity (V0018) and the Medical Research Council (MR/V006754/1). K.T., S.C.F.N and S.W.W. were supported by the UCL Neuroscience ZNZ Collaboration. L.E.V. was funded by FONDECYT grant (11160951), CONICYT International network grants (REDI170300 and REDES170010), and Universidad Mayor FDP grant (PEP I-2019074). CT, LEV and S.W. were supported by MRC grants (MR/L003775/1 and MR/T020164/1) to SW and Gaia Gestri and a Wellcome Trust investigator award to SW (104682/Z/14/Z). S.C.F.N. was supported by the Swiss National Science Foundation (31003A_173083) J.R. was supported by the BBSRC (BB/T001844/1) and Wellcome Trust (217150/Z/19/Z). E.B.N. was supported by core grants to the Wellcome Sanger Institute (WT098051 and 206194).

This publication presents independent research funded by the National Institute for Health Research (NIHR). The views expressed are those of the authors and not necessarily those of the NHS, the NIHR or the Department of Health and Social Care.

The funders had no role in study design, data collection and analysis, decision to publish, or preparation of the manuscript.

Competing interests:

The authors declare no competing interests.

Author contributions:

Conceptualization: K.T., E.M.B-N.; Data Curation: R.J.W., I.M.S.; Formal Analysis: K.T., R.J.W., I.H.B., I.M.S.; Investigation: K.T., R.J.W., C.T., L.E.V., S.N., I.H.B., R.G.-M., C.D., I.M.S.; Project Administration: K.T., E.M.B-N.; Supervision: L.E.V., S.C.F.N., J.R., C.H., S.W.W., E.M.B-N.; Validation: K.T.; Visualization: K.T., R.J.W.; Writing – Original Draft Preparation: K.T., R.J.W.; Writing – Review & Editing: L.E.V., S.N., I.H.B., R.G.-M., I.M.S., S.C.F.N., J.R., C.H., S.W.W., E.M.B-N.

References

Angeli S, Barhydt T, Jacobs R, Killilea DW, Lithgow GJ, Andersen JK (2014) Manganese disturbs metal and protein homeostasis in Caenorhabditis elegans. Metallomics 6:1816-1823.

Bauer S, Grossmann S, Vingron M, Robinson PN (2008) Ontologizer 2.0--a multifunctional tool for GO term enrichment analysis and data exploration. Bioinformatics 24:1650-1651.

Bindea G, Mlecnik B, Hackl H, Charoentong P, Tosolini M, Kirilovsky A, Fridman WH, Pages F, Trajanoski Z, Galon J (2009) ClueGO: a Cytoscape plug-in to decipher functionally grouped gene ontology and pathway annotation networks. Bioinformatics 25:1091-1093.

Blanc PD (2018) The early history of manganese and the recognition of its neurotoxicity, 1837-1936. Neurotoxicology 64:5-11.

Boycott KM et al. (2015) Autosomal-Recessive Intellectual Disability with Cerebellar Atrophy Syndrome Caused by Mutation of the Manganese and Zinc Transporter Gene SLC39A8. Am J Hum Genet 97:886-893.

Burton CE, Zhou Y, Bai Q, Burton EA (2017) Spectral properties of the zebrafish visual motor response. Neurosci Lett 646:62-67.

Caito S, Aschner M (2015) Neurotoxicity of metals. Handb Clin Neurol 131:169-189.

Chen P, Bornhorst J, Aschner M (2018) Manganese metabolism in humans. Front Biosci (Landmark Ed) 23:1655-1679.

Chino M, Leone L, Zambrano G, Pirro F, D'Alonzo D, Firpo V, Aref D, Lista L, Maglio O, Nastri F, Lombardi A (2018) Oxidation catalysis by iron and manganese porphyrins within enzyme-like cages. Biopolymers 109:e23107.

Choi HMT, Schwarzkopf M, Fornace ME, Acharya A, Artavanis G, Stegmaier J, Cunha A, Pierce NA (2018) Third-generation in situ hybridization chain reaction: multiplexed, quantitative, sensitive, versatile, robust. Development 145.

Collins JE, Wali N, Sealy IM, Morris JA, White RJ, Leonard SR, Jackson DK, Jones MC, Smerdon NC, Zamora J, Dooley CM, Carruthers SN, Barrett JC, Stemple DL, Busch-Nentwich EM (2015) High-throughput and quantitative genome-wide messenger RNA sequencing for molecular phenotyping. BMC Genomics 16:578.

Fairless R, Williams SK, Diem R (2019) Calcium-Binding Proteins as Determinants of Central Nervous System Neuronal Vulnerability to Disease. Int J Mol Sci 20.

Fernandes AM, Fero K, Arrenberg AB, Bergeron SA, Driever W, Burgess HA (2012) Deep brain photoreceptors control light-seeking behavior in zebrafish larvae. Curr Biol 22:2042-2047.

Fordahl SC, Erikson KM (2014) Manganese accumulation in membrane fractions of primary astrocytes is associated with decreased gamma-aminobutyric acid (GABA) uptake, and is exacerbated by oleic acid and palmitate. Environ Toxicol Pharmacol 37:1148-1156.

Ghosh M, Rihel J (2020) Hierarchical Compression Reveals Sub-Second to Day-Long Structure in Larval Zebrafish Behavior. eNeuro 7.

Gong H, Amemiya T (1996) Ultrastructure of retina of manganese-deficient rats. Invest Ophthalmol Vis Sci 37:1967-1974.

Gorojod RM, Alaimo A, Porte Alcon S, Saravia F, Kotler ML (2017) Interplay between lysosomal, mitochondrial and death receptor pathways during manganese-induced apoptosis in glial cells. Arch Toxicol 91:3065-3078.

Gorojod RM, Alaimo A, Porte Alcon S, Martinez JH, Cortina ME, Vazquez ES, Kotler ML (2018) Heme Oxygenase-1 protects astroglia against manganese-induced oxidative injury by regulating mitochondrial quality control. Toxicol Lett 295:357-368.

Groenendyk J, Agellon LB, Michalak M (2021) Calcium signaling and endoplasmic reticulum stress. Int Rev Cell Mol Biol 363:1-20.

Guilarte TR, Gonzales KK (2015) Manganese-Induced Parkinsonism Is Not Idiopathic Parkinson's Disease: Environmental and Genetic Evidence. Toxicol Sci 146:204-212.

Gupta T, Marquart GD, Horstick EJ, Tabor KM, Pajevic S, Burgess HA (2018) Morphometric analysis and neuroanatomical mapping of the zebrafish brain. Methods 150:49-62.

Harischandra DS, Ghaisas S, Zenitsky G, Jin H, Kanthasamy A, Anantharam V, Kanthasamy AG (2019a) Manganese-Induced Neurotoxicity: New Insights Into the Triad of Protein Misfolding, Mitochondrial Impairment, and Neuroinflammation. Front Neurosci 13:654.

Harischandra DS, Rokad D, Neal ML, Ghaisas S, Manne S, Sarkar S, Panicker N, Zenitsky G, Jin H, Lewis M, Huang X, Anantharam V, Kanthasamy A, Kanthasamy AG (2019b) Manganese promotes the aggregation and prion-like cell-to-cell exosomal transmission of alpha-synuclein. Sci Signal 12.

Hasegawa S, Kumagai M, Hagihara M, Nishimaru H, Hirano K, Kaneko R, Okayama A, Hirayama T, Sanbo M, Hirabayashi M, Watanabe M, Hirabayashi T, Yagi T (2016) Distinct and Cooperative Functions for the Protocadherin-alpha, -beta and -gamma Clusters in Neuronal Survival and Axon Targeting. Front Mol Neurosci 9:155.

Heinz S, Benner C, Spann N, Bertolino E, Lin YC, Laslo P, Cheng JX, Murre C, Singh H, Glass CK (2010) Simple combinations of lineage-determining transcription factors prime cis-regulatory elements required for macrophage and B cell identities. Mol Cell 38:576-589.

Hernandez RB, Moteshareie H, Burnside D, McKay B, Golshani A (2019) Manganese-induced cellular disturbance in the baker's yeast, Saccharomyces cerevisiae with putative implications in neuronal dysfunction. Sci Rep 9:6563.

Hertz E, Terenius L, Vukojevic V, Svenningsson P (2019) GPR37 and GPR37L1 differently interact with dopamine 2 receptors in live cells. Neuropharmacology 152:51-57.

Hong CJ, Yeon J, Yeo BK, Woo H, An HK, Heo W, Kim K, Yu SW (2020) Fas-apoptotic inhibitory molecule 2 localizes to the lysosome and facilitates autophagosome-lysosome fusion through the LC3 interaction region motif-dependent interaction with LC3. FASEB J 34:161-179.

Ijomone OM, Miah MR, Peres TV, Nwoha PU, Aschner M (2016) Null allele mutants of trt-1, the catalytic subunit of telomerase in Caenorhabditis elegans, are less sensitive to Mn-induced toxicity and DAergic degeneration. Neurotoxicology 57:54-60.

Jadiya P, Garbincius JF, Elrod JW (2021) Reappraisal of metabolic dysfunction in neurodegeneration: Focus on mitochondrial function and calcium signaling. Acta Neuropathol Commun 9:124.

Juneja M, Shamim U, Joshi A, Mathur A, Uppili B, Sairam S, Ambawat S, Dixit R, Faruq M (2018) A novel mutation in SLC39A14 causing hypermanganesemia associated with infantile onset dystonia. J Gene Med 20:e3012.

Kalbitzer HR, Stehlik D, Hasselbach W (1978) The binding of calcium and magnesium to sarcoplasmic reticulum vesicles as studied by manganese electron paramagnetic resonance. Eur J Biochem 82:245-255.

Kaupp UB, Seifert R (2002) Cyclic nucleotide-gated ion channels. Physiol Rev 82:769-824.

Kikuchihara Y, Abe H, Tanaka T, Kato M, Wang L, Ikarashi Y, Yoshida T, Shibutani M (2015) Relationship between brain accumulation of manganese and aberration of hippocampal adult neurogenesis after oral exposure to manganese chloride in mice. Toxicology 331:24-34.

Kim SY, Yasuda S, Tanaka H, Yamagata K, Kim H (2011) Non-clustered protocadherin. Cell Adh Migr 5:97-105.

Kimmel CB, Ballard WW, Kimmel SR, Ullmann B, Schilling TF (1995) Stages of embryonic development of the zebrafish. Dev Dyn 203:253-310.

Koller WC, Lyons KE, Truly W (2004) Effect of levodopa treatment for parkinsonism in welders: A double-blind study. Neurology 62:730-733.

Lee JH, Shin JH (2022) Effect of Chelation Therapy on a Korean Patient With Brain Manganese Deposition Resulting From a Compound Heterozygous Mutation in the SLC39A14 Gene. J Mov Disord.

Leung KW, Liu M, Xu X, Seiler MJ, Barnstable CJ, Tombran-Tink J (2008) Expression of ZnT and ZIP zinc transporters in the human RPE and their regulation by neurotrophic factors. Invest Ophthalmol Vis Sci 49:1221-1231.

Li H, Durbin R (2009) Fast and accurate short read alignment with Burrows-Wheeler transform. Bioinformatics 25:1754-1760.

Li H, Fan X, Luo Y, Song S, Liu J, Fan Q (2017) Repeated manganese administration produced abnormal expression of circadian clock genes in the hypothalamus and liver of rats. Neurotoxicology 62:39-45.

Livak KJ, Schmittgen TD (2001) Analysis of relative gene expression data using real-time quantitative PCR and the 2(-Delta Delta C(T)) Method. Methods 25:402-408.

Love MI, Huber W, Anders S (2014) Moderated estimation of fold change and dispersion for RNA-seq data with DESeq2. Genome Biol 15:550.

Luo X, Liu Z, Ge X, Huang S, Zhou Y, Li D, Li L, Chen X, Huang L, Hou Q, Cheng H, Xiao L, Liu C, Zou Y, Yang X (2020) High manganese exposure decreased the risk of high triglycerides in workers: a cross-sectional study. BMC Public Health 20:874.

Mancini M, Bassani S, Passafaro M (2020) Right Place at the Right Time: How Changes in Protocadherins Affect Synaptic Connections Contributing to the Etiology of Neurodevelopmental Disorders. Cells 9.

Marquart GD, Tabor KM, Horstick EJ, Brown M, Geoca AK, Polys NF, Nogare DD, Burgess HA (2017) High-precision registration between zebrafish brain atlases using symmetric diffeomorphic normalization. Gigascience 6:1-15.

Marquart GD, Tabor KM, Brown M, Strykowski JL, Varshney GK, LaFave MC, Mueller T, Burgess SM, Higashijima S, Burgess HA (2015) A 3D Searchable Database of Transgenic Zebrafish Gal4 and Cre Lines for Functional Neuroanatomy Studies. Front Neural Circuits 9:78.

Marreilha Dos Santos AP, Andrade V, Aschner M (2017) Neuroprotective and Therapeutic Strategies for Manganese-Induced Neurotoxicity. Clin Pharmacol Transl Med 1:54-62.

Marti-Sanchez L, Ortigoza-Escobar JD, Darling A, Villaronga M, Baide H, Molero-Luis M, Batllori M, Vanegas MI, Muchart J, Aquino L, Artuch R, Macaya A, Kurian MA, Duenas P (2018) Hypermanganesemia due to mutations in SLC39A14: further insights into Mn deposition in the central nervous system. Orphanet J Rare Dis 13:28.

Martinez-Finley EJ, Gavin CE, Aschner M, Gunter TE (2013) Manganese neurotoxicity and the role of reactive oxygen species. Free Radic Biol Med.

Mueller KP, Neuhauss SC (2014) Sunscreen for fish: co-option of UV light protection for camouflage. PLoS One 9:e87372.

Nakamura T, Oh CK, Zhang X, Lipton SA (2021) Protein S-nitrosylation and oxidation contribute to protein misfolding in neurodegeneration. Free Radic Biol Med 172:562-577.

Nara M, Tasumi M, Tanokura M, Hiraoki T, Yazawa M, Tsutsumi A (1994) Infrared studies of interaction between metal ions and Ca(2+)-binding proteins. Marker bands for identifying the types of coordination of the side-chain COO- groups to metal ions in pike parvalbumin (pI = 4.10). FEBS Lett 349:84-88.

Octeau JC, Schrader JM, Masuho I, Sharma M, Aiudi C, Chen CK, Kovoor A, Celver J (2014) G protein beta 5 is targeted to D2-dopamine receptor-containing biochemical compartments and blocks dopamine-dependent receptor internalization. PLoS One 9:e105791.

Ou CY, Luo YN, He SN, Deng XF, Luo HL, Yuan ZX, Meng HY, Mo YH, Li SJ, Jiang YM (2017) Sodium P-Aminosalicylic Acid Improved Manganese-Induced Learning and Memory Dysfunction via Restoring the Ultrastructural Alterations and gamma-Aminobutyric Acid Metabolism Imbalance in the Basal Ganglia. Biol Trace Elem Res 176:143-153.

Park JH et al. (2015) SLC39A8 Deficiency: A Disorder of Manganese Transport and Glycosylation. Am J Hum Genet 97:894-903.

Popichak KA, Afzali MF, Kirkley KS, Tjalkens RB (2018) Glial-neuronal signaling mechanisms underlying the neuroinflammatory effects of manganese. J Neuroinflammation 15:324.

Porte Alcon S, Gorojod RM, Kotler ML (2018) Regulated Necrosis Orchestrates Microglial Cell Death in Manganese-Induced Toxicity. Neuroscience 393:206-225.

Quintanar L, Montiel T, Marquez M, Gonzalez A, Massieu L (2012) Calpain activation is involved in acute manganese neurotoxicity in the rat striatum in vivo. Exp Neurol 233:182-192.

Randlett O, Wee CL, Naumann EA, Nnaemeka O, Schoppik D, Fitzgerald JE, Portugues R, Lacoste AM, Riegler C, Engert F, Schier AF (2015) Whole-brain activity mapping onto a zebrafish brain atlas. Nat Methods 12:1039-1046.

Rao MV, Zaidel-Bar R (2016) Formin-mediated actin polymerization at cell-cell junctions stabilizes E-cadherin and maintains monolayer integrity during wound repair. Mol Biol Cell 27:2844-2856.

Rihel J, Prober DA, Arvanites A, Lam K, Zimmerman S, Jang S, Haggarty SJ, Kokel D, Rubin LL, Peterson RT, Schier AF (2010) Zebrafish behavioral profiling links drugs to biological targets and rest/wake regulation. Science 327:348-351.

Rizor A, Pajarillo E, Nyarko-Danquah I, Digman A, Mooneyham L, Son DS, Aschner M, Lee E (2021) Manganese-induced reactive oxygen species activate IkappaB kinase to upregulate YY1 and impair glutamate transporter EAAT2 function in human astrocytes in vitro. Neurotoxicology 86:94-103.

Rodan LH, Hauptman M, D'Gama AM, Qualls AE, Cao S, Tuschl K, Al-Jasmi F, Hertecant J, Hayflick SJ, Wessling-Resnick M, Yang ET, Berry GT, Gropman A, Woolf AD, Agrawal PB (2018) Novel founder intronic variant in SLC39A14 in two families causing Manganism and potential treatment strategies. Mol Genet Metab 124:161-167.

Sidoryk-Wegrzynowicz M, Aschner M (2013) Manganese toxicity in the central nervous system: the glutamine/glutamate-gamma-aminobutyric acid cycle. J Intern Med 273:466-477.

Sirri F, Maiorano G, Tavaniello S, Chen J, Petracci M, Meluzzi A (2016) Effect of different levels of dietary zinc, manganese, and copper from organic or inorganic sources on performance, bacterial chondronecrosis, intramuscular collagen characteristics, and occurrence of meat quality defects of broiler chickens. Poult Sci 95:1813-1824.

Smith MR, Fernandes J, Go YM, Jones DP (2017) Redox dynamics of manganese as a mitochondrial life-death switch. Biochem Biophys Res Commun 482:388-398.

Soares ATG, Silva AC, Tinkov AA, Khan H, Santamaria A, Skalnaya MG, Skalny AV, Tsatsakis A, Bowman AB, Aschner M, Avila DS (2020) The impact of manganese on neurotransmitter systems. J Trace Elem Med Biol 61:126554.

Song D, Ma J, Chen L, Guo C, Zhang Y, Chen T, Zhang S, Zhu Z, Tian L, Niu P (2017) FOXO3 promoted mitophagy via nuclear retention induced by manganese chloride in SH-SY5Y cells. Metallomics 9:1251-1259.

Taka E, Mazzio E, Soliman KF, Renee RR (2012) Microarray genomic profile of mitochondrial and oxidant response in manganese chloride treated PC12 cells. Neurotoxicology 33:162-168.

Tamas MJ, Sharma SK, Ibstedt S, Jacobson T, Christen P (2014) Heavy metals and metalloids as a cause for protein misfolding and aggregation. Biomolecules 4:252-267.

Thompson KJ, Wessling-Resnick M (2019) ZIP14 is degraded in response to manganese exposure. Biometals 32:829-843.

Tinkov AA, Paoliello MMB, Mazilina AN, Skalny AV, Martins AC, Voskresenskaya ON, Aaseth J, Santamaria A, Notova SV, Tsatsakis A, Lee E, Bowman AB, Aschner M (2021) Molecular Targets of Manganese-Induced Neurotoxicity: A Five-Year Update. Int J Mol Sci 22.

Tjalkens RB, Popichak KA, Kirkley KA (2017) Inflammatory Activation of Microglia and Astrocytes in Manganese Neurotoxicity. Adv Neurobiol 18:159-181.

Tuschl K, Clayton PT, Gospe SM, Mills PB (1993) Dystonia/Parkinsonism, Hypermanganesemia, Polycythemia, and Chronic Liver Disease.

Tuschl K, Mills PB, Parsons H, Malone M, Fowler D, Bitner-Glindzicz M, Clayton PT (2008) Hepatic cirrhosis, dystonia, polycythaemia and hypermanganesaemia--a new metabolic disorder. J Inherit Metab Dis 31:151-163.

Tuschl K, Clayton PT, Gospe SM, Jr., Gulab S, Ibrahim S, Singhi P, Aulakh R, Ribeiro RT, Barsottini OG, Zaki MS, Del Rosario ML, Dyack S, Price V, Rideout A, Gordon K, Wevers RA, Chong WK, Mills PB (2012) Syndrome of hepatic cirrhosis, dystonia, polycythemia, and hypermanganesemia caused by mutations in SLC30A10, a manganese transporter in man. Am J Hum Genet 90:457-466.

Tuschl K et al. (2016) Mutations in SLC39A14 disrupt manganese homeostasis and cause childhood-onset parkinsonism-dystonia. Nat Commun 7:11601.

Wang C, Ma Z, Yan DY, Liu C, Deng Y, Liu W, Xu ZF, Xu B (2018) Alpha-Synuclein and Calpains Disrupt SNARE-Mediated Synaptic Vesicle Fusion During Manganese Exposure in SH-SY5Y Cells. Cells 7.

Wang D, Zhang J, Jiang W, Cao Z, Zhao F, Cai T, Aschner M, Luo W (2017) The role of NLRP3-CASP1 in inflammasome-mediated neuroinflammation and autophagy dysfunction in manganese-induced, hippocampal-dependent impairment of learning and memory ability. Autophagy 13:914-927.

Wang WA, Groenendyk J, Michalak M (2012) Calreticulin signaling in health and disease. Int J Biochem Cell Biol 44:842-846.

Xu B, Shan M, Wang F, Deng Y, Liu W, Feng S, Yang TY, Xu ZF (2013) Endoplasmic reticulum stress signaling involvement in manganese-induced nerve cell damage in organotypic brain slice cultures. Toxicol Lett 222:239-246.

Yates AD et al. (2020) Ensembl 2020. Nucleic Acids Res 48:D682-D688.

Zeglam A, Abugrara A, Kabuka M (2018) Autosomal-recessive iron deficiency anemia, dystonia and hypermanganesemia caused by new variant mutation of the manganese transporter gene SLC39A14. Acta Neurol Belg.

Zhi CN, Lai LL, Dou CS, Wang XH, Zhao P, Fu JL, Yao BY (2019) [The role of lysosomes in manganese-induced toxicity in SK-N-SH cells]. Zhonghua Lao Dong Wei Sheng Zhi Ye Bing Za Zhi 37:332-336.

Zofkova I, Davis M, Blahos J (2017) Trace elements have beneficial, as well as detrimental effects on bone homeostasis. Physiol Res 66:391-402.

Zou Y, Qing L, Zeng X, Shen Y, Zhong Y, Liu J, Li Q, Chen K, Lv Y, Huang D, Liang G, Zhang W, Chen L, Yang Y, Yang X (2014) Cognitive function and plasma BDNF levels among manganese-exposed smelters. Occup Environ Med 71:189-194.

Figures and Table

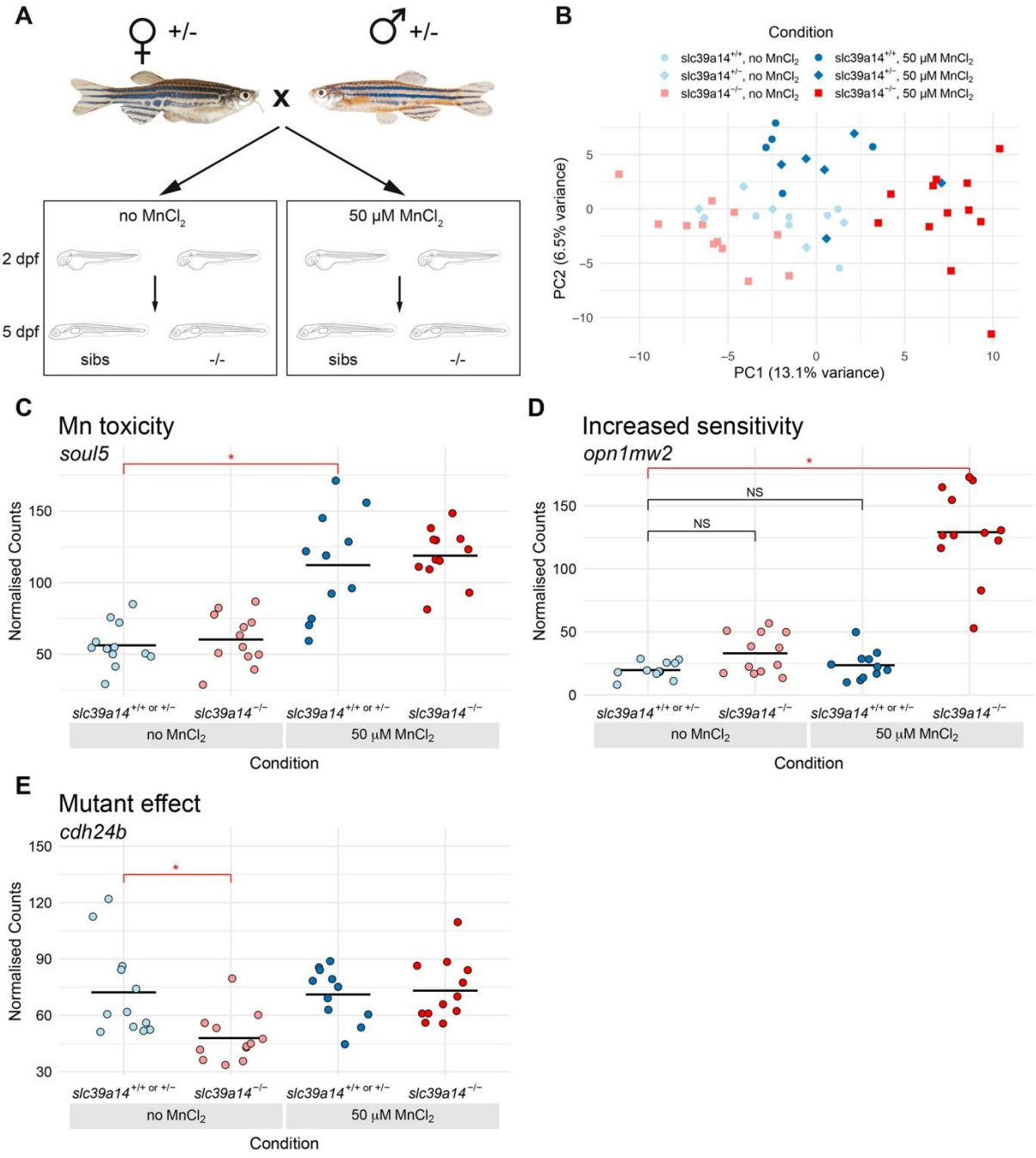

Fig. 1. DeTCT analysis identifies three groups of differentially expressed genes.

(A) Diagram of the experiment. Embryos from a *slc39a14*$^{+/-}$ incross were either left unexposed or exposed to 50µM $MnCl_2$ from 2 to 5 dpf.

(B) Principal Component Analysis of the samples. Principal component (PC) 1 is plotted on the x-axis and PC2 on the y-axis. Samples belonging to the same condition group together.

circles = wild-type embryos, diamonds = heterozygotes, squares = homozygote mutants. Unexposed sibling embryos are light blue and $MnCl_2$ exposed ones are dark blue. Unexposed mutants are coloured light red and exposed mutants are dark red.

(C) Group 1 (Mn toxicity) genes are defined as those with a significant difference between exposed and unexposed siblings (red bar with asterisk). Example plot of normalised counts for the *soul5* gene. The colour scheme for C–E is the same as in (B).

(D) Group 2 (Increased sensitivity) genes are defined as those with a significant difference between exposed mutants and unexposed siblings (red bar with asterisk) without significant differences in either unexposed mutants or exposed siblings when compared to unexposed siblings (black bars labelled NS). Example plot of normalised counts for the *opn1mw2* gene.

(E) Group3 (Mutant effect) is defined as genes with a significant difference between unexposed mutants and unexposed siblings (red bar with asterisk). Example plot of normalised counts for the *cdh24b* gene.

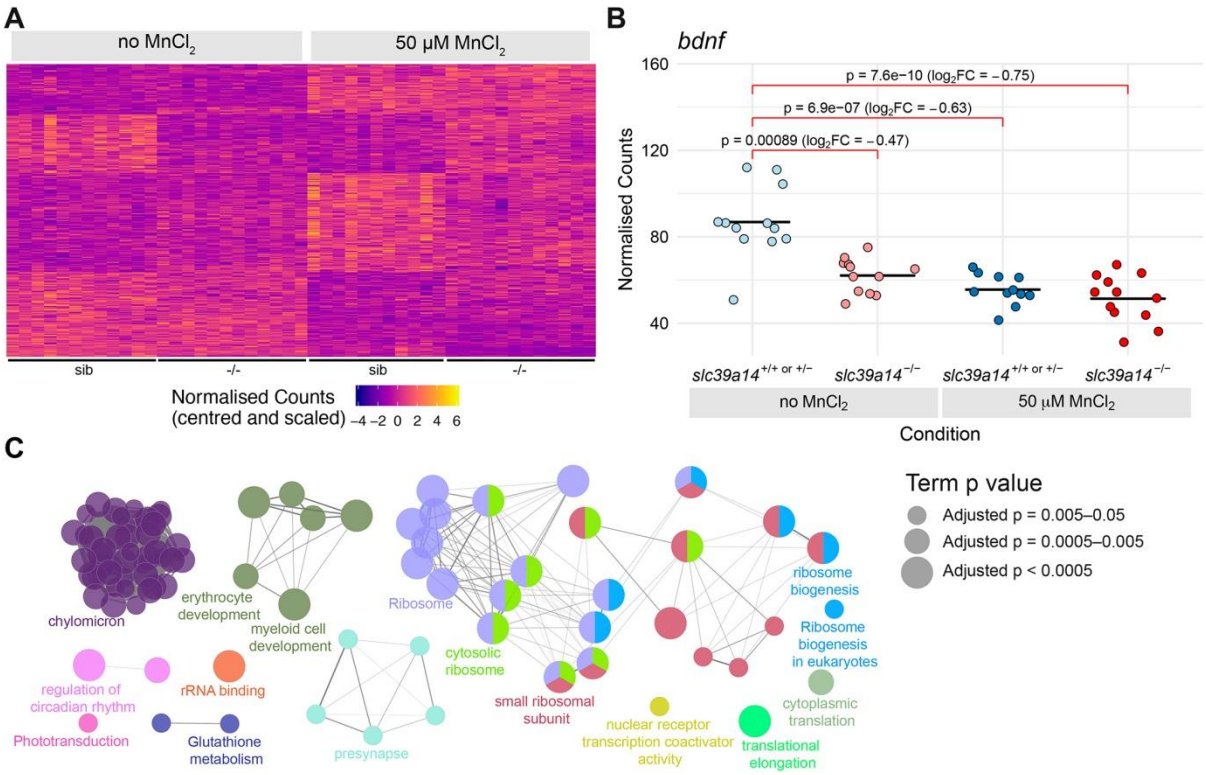

Fig. 2. Manganese overexposure causes neurotoxicity and metabolic defects in *slc39a14*$^{+/+}$ *or*$^{+/-}$ embryos.

(A) Heatmap of the expression of all 328 genes with a significant difference between exposed and unexposed siblings (Group 1 - Mn toxicity, Table S1). Each row represents a different gene and each column is a sample. Mutant embryos are displayed for completeness although the group of genes is defined by the response in siblings only. The normalised counts for each gene have been mean centred and scaled by dividing by the standard deviation.

(B) Plot of the normalised counts for each sample of a gene (*bdnf*) in Group 1. Unexposed sibling embryos are light blue and $MnCl_2$ exposed ones are dark blue. Unexposed mutants are coloured light red and exposed mutants are dark red.

(C) Enrichment of Gene Ontology (GO) terms associated with the genes in (A). Diagram produced using the CytoScape ClueGO App. Nodes represent enriched GO terms and edges connect GO terms that have annotated genes in common. Different components of the network are coloured according to the categories labelled on the diagram. See Figure S1 for GO enrichment split by up- and downregulation.

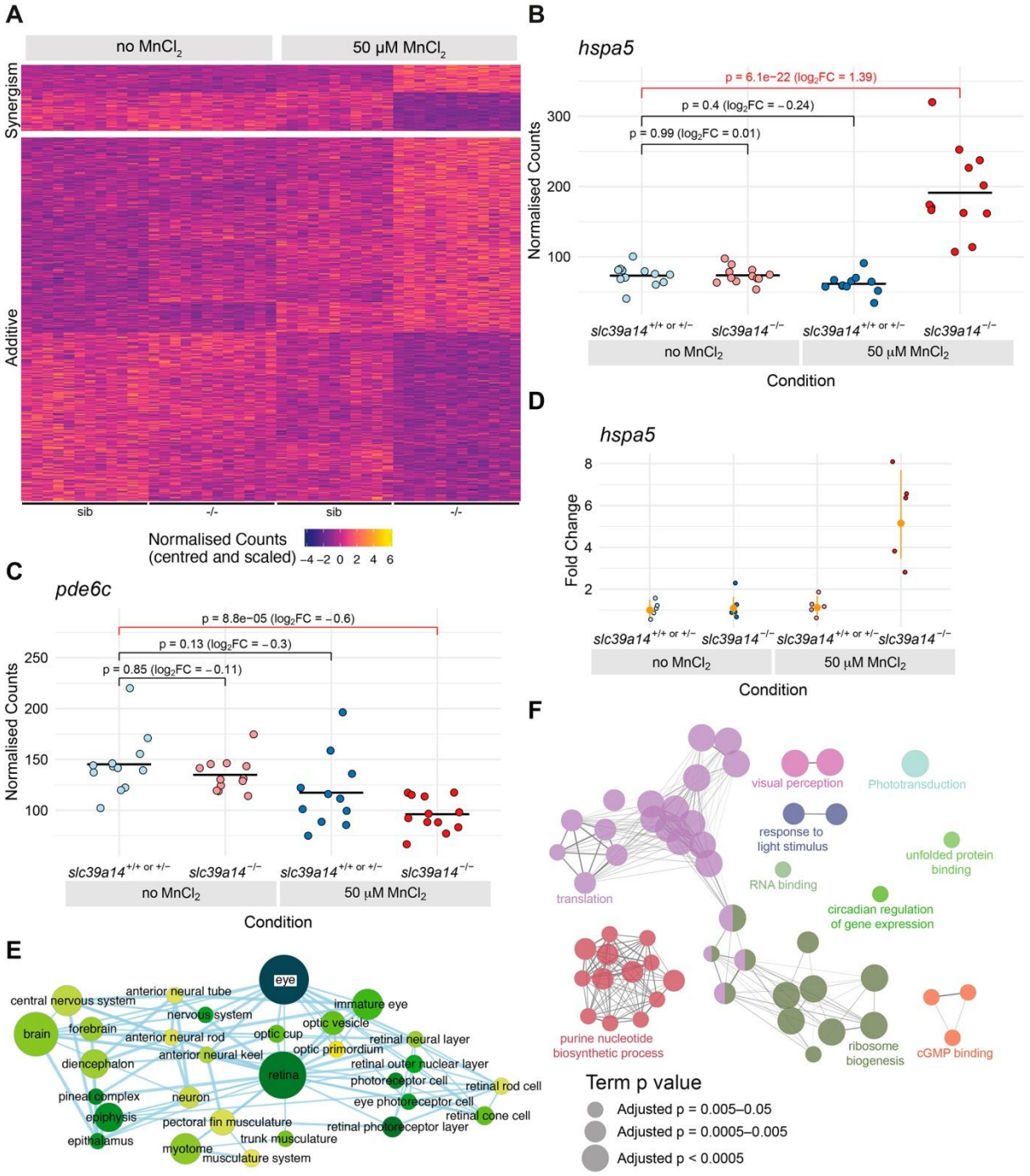

Fig. 3. Effect of Mn treatment in *slc39a14*$^{-/-}$ mutants.

(A) Heatmap of the expression of all genes (613) with a significant difference between exposed mutant and unexposed sibling embryos without significant treatment or genotype effects. The heatmaps are split into genes that show either synergistic or additive effects of the individual genotype and treatment effects. Each row represents a different gene and

each column is a sample. The normalised counts for each gene have been mean centred and scaled by dividing by the standard deviation.

(B) Example of a gene (*hspa5*) with a synergistic effect of treatment and genotype. The difference between the exposed mutants and unexposed siblings cannot be explained by adding together the separate effects of Mn treatment and the *slc39a14*$^{-/-}$ mutation. Unexposed sibling embryos are light blue and $MnCl_2$ exposed ones are dark blue. Unexposed mutants are coloured light red and exposed mutants are dark red.

(C) Example of a gene (*pde6c*) that has an additive effect of treatment and genotype. The difference between exposed mutants and unexposed siblings is consistent with adding together the two sub-threshold effects of treatment and genotype produce. Colour scheme as in (B).

(D) qRT-PCR shows comparable gene expression changes for *hspa5* as for the single embryo sequencing dataset. The individual samples are displayed as fold change relative to the mean value for unexposed siblings and the mean and 95% confidence intervals for each condition are in orange. Compare with (B).

(E) Enrichment Map network of the Zebrafish Anatomy Ontology (ZFA) enrichment results. Each node represents an enriched ZFA term and the edges join nodes that have overlapping genes annotated to them. The width of each edge is proportional to amount of overlap, nodes are coloured by $-\log_{10}$[Adjusted p value] and the size represents the number of significant genes annotated to the term.

(F) ClueGO network diagram of the enrichment of Gene Ontology (GO) terms. Nodes represent enriched GO terms and edges connect nodes that share annotations to the significant genes. Different components of the network are coloured according to the categories as labelled on the diagram.

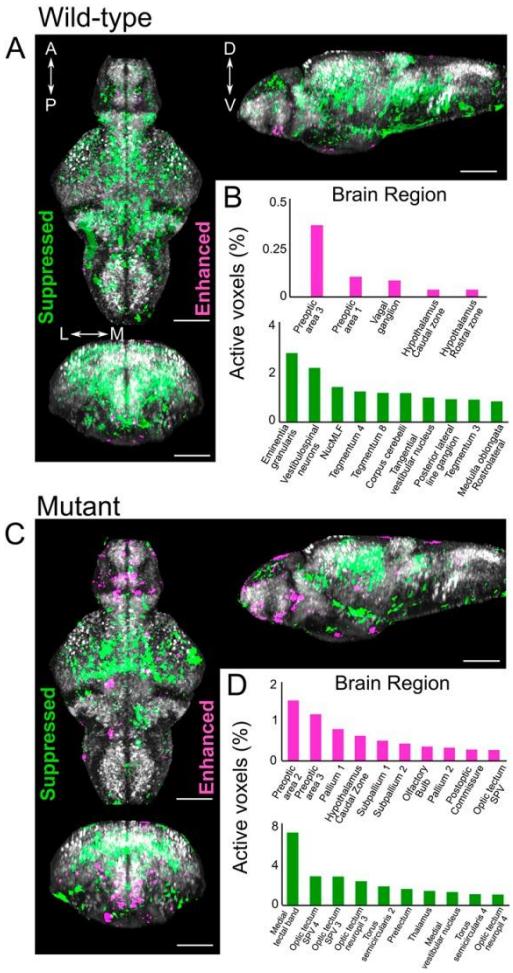

Fig. 4. $MnCl_2$ treatment alters neuronal activity in both wild-type and *slc39a14*$^{-/-}$ larvae. Z projection of *cfos* mRNA expression in the brain of (A) wild-type and (C) homozygous mutant larvae at 6 dpf following treatment with 50µM $MnCl_2$ from 2 dpf. (B) and (D) list the brain regions with enhanced (magenta) and reduced (green) neuronal activity by genotype. A, anterior; P, posterior; D, dorsal; V, ventral.

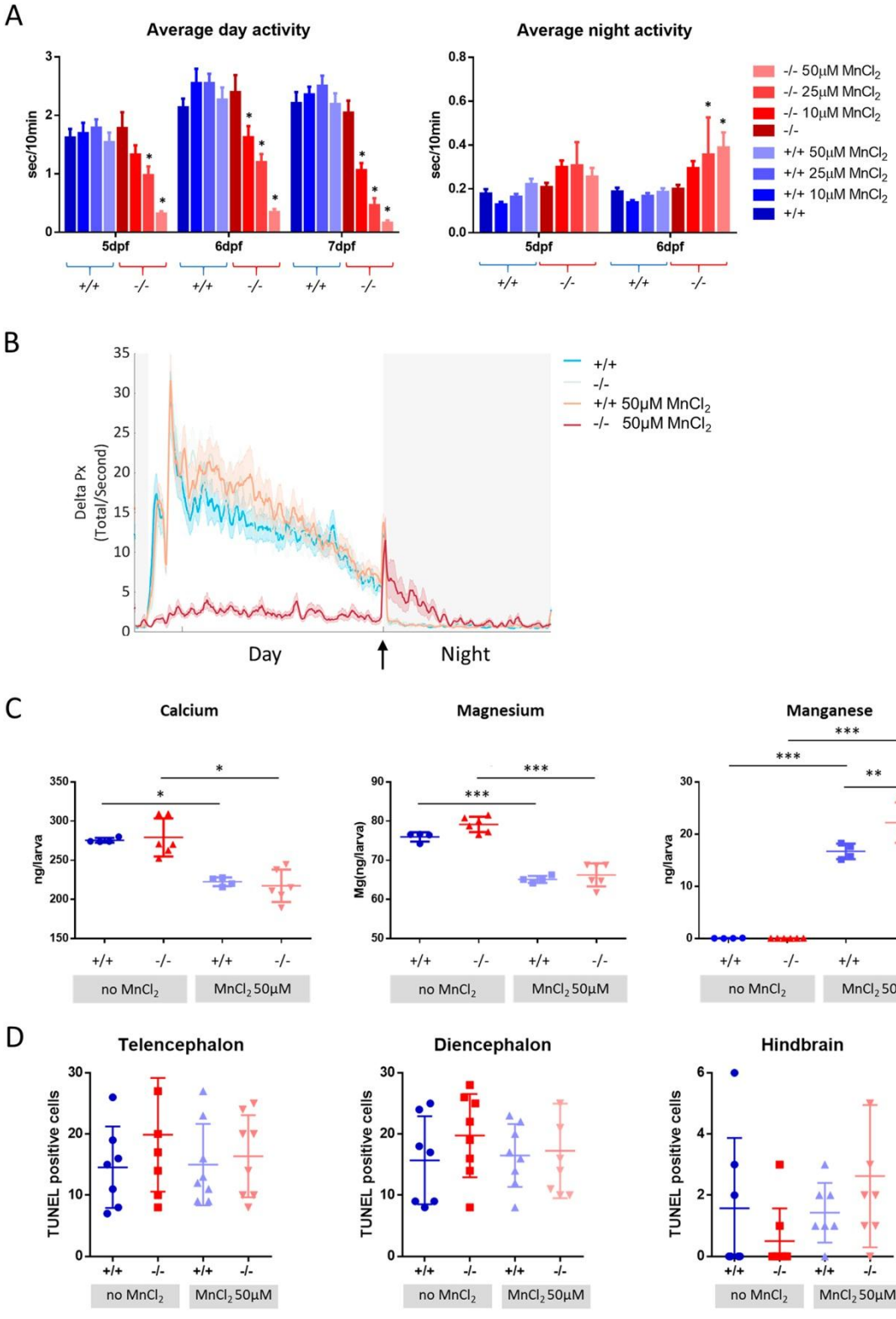

Fig. 5. $MnCl_2$ treatment causes locomotor abnormalities and calcium dyshomeostasis.

(A) Average locomotor activity of wild-type (blue) and *slc39a14*$^{-/-}$ larvae (red) during the day and night in response to increasing concentrations of $MnCl_2$. Data are presented as mean ± SEM. (Two-way ANOVA with Tukey's posthoc test; *, $p<0.05$), n=24 larvae per group.

(B) Frame-by-frame analysis of the locomotor activity of wild-type and *slc39a14*$^{-/-}$ larvae at 6 dpf unexposed and exposed to 50µM $MnCl_2$. White shading representing the day (lights ON) and grey shading the night (lights OFF). Arrow indicating lights OFF switch. Shown is a summed and smoothed mean Δ pixels trace (bold line) ± s.e.m. (shaded surround). n=24 larvae per group.

(C) Calcium, magnesium and manganese concentrations determined by ICP-MS in untreated and $MnCl_2$ (50µM) treated wild-type and *slc39a14*$^{-/-}$ larvae. Data are presented as mean ± s.d. (One-way ANOVA with Tukey's posthoc test; *, $p<0.05$; **, $p<0.01$; ***, $p<0.001$).

(D) Apoptotic cell death upon $MnCl_2$ exposure in both wild-type (blue) and mutant (red) larvae at 5dpf detected by TUNEL staining in the telencephalon, diencephalon and hindbrain. Data are presented as mean ± s.d.

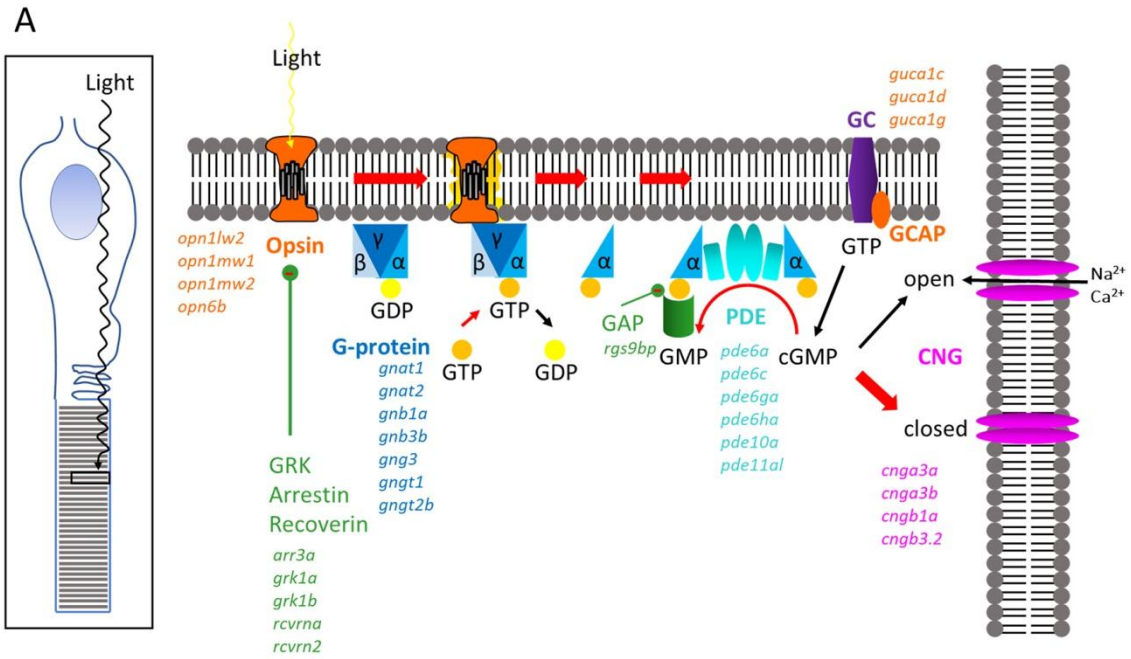

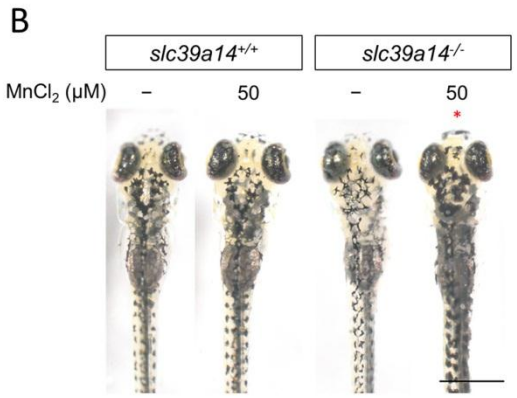

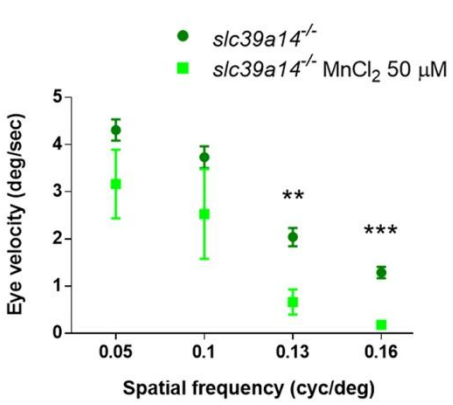

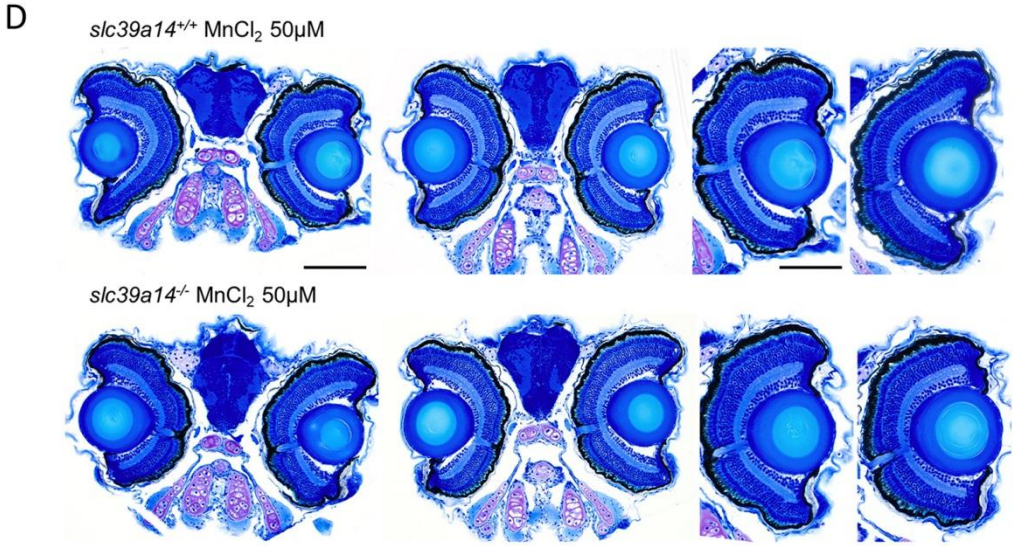

Fig. 6. *slc39a14*$^{-/-}$ mutants develop a visual phenotype upon $MnCl_2$ exposure. (A) Schematic showing the process of phototransduction (Kaupp and Seifert, 2002) with differentially expressed genes observed in $MnCl_2$ exposed *slc39a14*$^{-/-}$ mutants in italics. cGMP, cyclic guanosine monophosphate. CNG, cyclic nucleotide gated non-selective cation channels. GC, guanylyl cyclase. GCAP, guanylate cyclase activating protein. PDE, phosphodiesterase. GRK, G-protein coupled receptor kinase. GAP, GTPase activating protein.

(B) Dorsal views during light exposure of wild-type siblings (*slc39a14*$^{+/+}$, on the left) and *slc39a14*$^{-/-}$ larvae (on the right) at 5 dpf unexposed and exposed to 50µM $MnCl_2$. * Note the darker pigmentation of mutants exposed to $MnCl_2$. Scale bar 500µm.

(C) Graph showing the eye velocity in response to moving stimuli of different spatial frequencies (average of both eyes) of *slc39a14*$^{-/-}$ larvae unexposed (dark green squares) and exposed to 50µM $MnCl_2$ (light green circles). Data are presented as mean ± s.e.m. from five independent experiments. (Student's t-test; **p<0.01; *** p<0.001).

(D) Histologic analysis of retinal sections with Richardson–Romeis staining of wild-type siblings (*slc39a14*$^{+/+}$, top row) and *slc39a14*$^{-/-}$ larvae (bottom row) at 5 dpf exposed to 50µM $MnCl_2$.

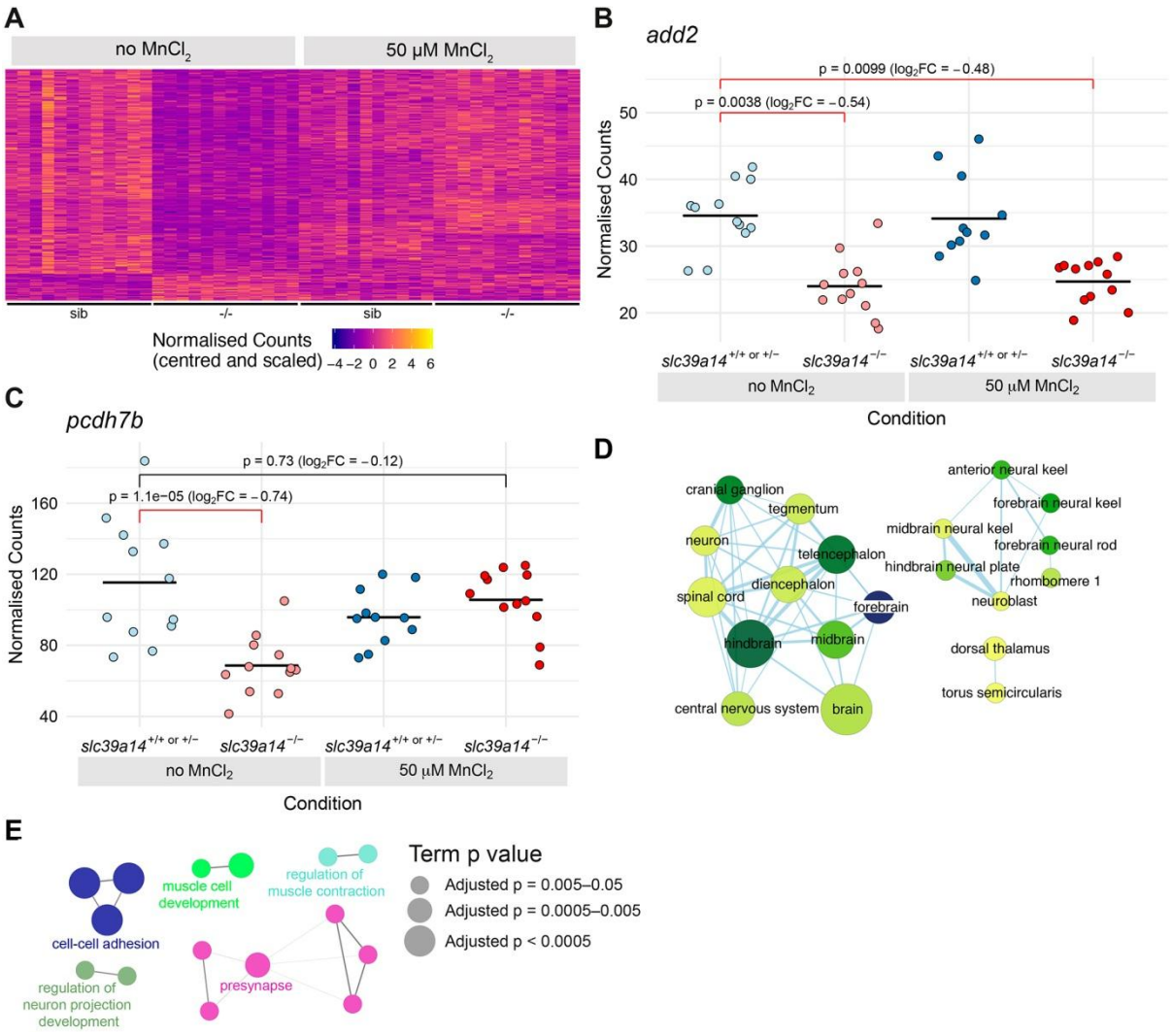

Fig. 7. Exogenous Mn restores normal expression of genes differentially expressed in unexposed *slc39a14*$^{-/-}$ mutants.

(A) Heatmap of the expression of 266 genes with a significant difference between unexposed mutants and unexposed siblings. Each row represents a different gene and each column is a sample. The normalised counts for each gene have been mean centred and scaled by dividing by the standard deviation.

(B) Plot of normalised counts for the *add2* gene. Expression is decreased in both unexposed and $MnCl_2$ exposed mutant embryos. Unexposed sibling embryos are light blue and Mn-exposed ones are dark blue. Unexposed mutants are coloured light red and exposed mutants are dark red.

(C) Plot of normalised counts for the *pcdh7b* gene. There are decreased counts in the unexposed mutant embryos that are rescued back to wild-type levels upon 50 µM $MnCl_2$ treatment. Colour scheme as in (B).

(D) Enrichment Map diagram of the enrichment of Zebrafish Anatomy Ontology (ZFA) terms for the genes differentially expressed in unexposed mutants that are rescued by Mn treatment. Nodes represent enriched ZFA terms and edges connect nodes that share annotations to the significant genes. The width of each edge is proportional to amount of overlap, nodes are coloured by $-\log_{10}$[Adjusted p value] and the size represents the number of significant genes annotated to the term.

(E) ClueGO network diagram of the enrichment of Gene Ontology (GO) terms associated with the genes that are rescued by Mn treatment. Nodes represent enriched GO terms and edges connect nodes that share annotations to the significant genes. Different components of the network are coloured according to the categories as labelled on the diagram.

Table 1. Differentially expressed genes grouped by function.

Mn toxicity independent of genotype	**Increased sensitivity** of *slc39a14*$^{-/-}$ mutants to $MnCl_2$ treatment	**Mutant effect** changes in *slc39a14*$^{-/-}$ mutants
Neuronal differentiation/growth *bdnf*	**Glutamate neurotransmission** *slc1a2a, slc1a2b, slc1a8a, nsg2, prrt1*	**Rescued by $MnCl_2$ treatment (Mn deficiency)**
GABA neurotransmission *pvalb2, pvalb8*	**GABA neurotransmission** *pvalb1, nptxrb, gabra6a, gabrb3, slc6a11b*	**Cell-cell adhesion - Ca^{2+}** *cdh24b, ctnnb1, pcdh1a, pcdh2g17, pcdh7b, pcdh9, pcdh10a, pcdh17, pcdh19*
Glutamate neurotransmission *grm8a*	**Dopaminergic neurotransmission** *gnb5b, gpr37l1b*	
Presynaptic neurotransmitter Release *rims2b, stxbp1a, sv2a, sypb, syt9a*	**Presynaptic neurotransmitter release** *rims2a, syngr1a, syt17*	**Cytoskeleton** *fhod3b, fnbp1a, fnbp4*
Signalling, axon guidance *efnb1, efnb2a*	**Astrocytes** *atf5a, atf5b, gfap*	**Muscle** *mef2aa, mef2cb, mtmr12, qkia, rbfox1, sgcd, tnnt3a, tnnt3b*
Ca^{2+} homeostasis *atp2a1, kcnn1a*	**Ca^{2+} homeostasis** *atp2a2b, atp2b1b, calr3, canx, camk1ga, camk2g1, camkva, capn7, dct, icn, ncaldb, pcdh7b, ppp3r1a, rgn, s100b, scpp1, tnni2a.4*	**Ca^{2+} homeostasis** *atp2a1, atp2b3b, cacnb4b, kcnma1a, kcnn1a, calm1b, calm3a, camta1b, strn4*
Inhibition of α-synuclein aggregation *sncb*		**Presynaptic neurotransmitter Release** *snap25a, sv2a, sypb, syt6a, syt9a*
Connective tissue *col2a1b, col4a5, col9a1, col9a2, col11a2, fbn2b, matn1*	**Unfolded protein response** *atf3, atf4b, atf6, derl1, dnajb11, herpud1, hspa5, hspd1, hspe1, syvn1, xbp1*	
Lipid metabolism *apoa4a, apoa4b.2, apoea*		**Neurite growth** *dock3, gas7a, kalrna, kalrnb, lrrc4c*
Porphyrin metabolism *alas1, fech, soul5*	**Autophagy** *glipr2l, hmgn2, rubcn, faim2b*	**Potassium channels** *kcnc1a, kcnc3a*
Thyroid function *dio3b*	**Apoptosis** *bri3bp, ppp1r13ba, taok2b, tmem214*	**Brain specific adhesion molecules** *cadm3, nlgn2b, nrcama, nrxn3a*
Ribosomal function *rpl11, rpl14, rpl23, rpl23a, rpl30, rpl32, rpl34, rpl35, rpl35a, rpl36, rpl36a, rpl38, rpl4, rpl5b, rpl7, rpl8, rpl9, rplp1, rplp2, rplp2l, rps10, rps11, rps12, rps13, rps14, rps15a, rps17, rps18, rps19, rps21, rps24, rps26l, rps28, rps3a, rps5*	**Ubiquitination / proteostasis** *otud5a, rer1, ube2l3b, ubqln4, ubtd1a, usp9, usp10, usp21*	**Ubiquitination / proteostasis** *birc6, fbxw11b, smurf2, serf2, stk40, ube2b, ube2ql1, vcp*
	Oxidative stress *prdx1, txn, txnrd3*	
	Ribosomal function & translation *rrp8, rrp12, rplp2, rps7, rps20, mrps30, eif1axb, eif4a1a, eif4bb, eif4e1c, eif4g1a, eif4h, eif5b, aars, cars, farsa, gars, kars, larsb, mars, nars, sars, yars*	**Not rescued by $MnCl_2$ treatment**
Circadian rhythm *cipca, cry1aa, cry1bb, cryba4, nr1d1, nr1d2a, nr1d4b, per1b, per3*		**Neuronal differentiation/growth** *bdnf*
	Lysosomal function *ctsd, ctsk, ctsla, ctsll, lgmn*	**Presynaptic neurotransmitter release** *rims2b, sypa*
	Wnt/β-catenin signalling *amer2, dact1*	**Ca^{2+} homeostasis** *atp2a1*
	Akt/PI3K/mTOR signalling *pik3c2b, pik3r1, pik3r3a, pik3r3b, rhebl1*	**Porphyrin metabolism** *alas1*
	Purine and pyrimidine metabolism *adssl1, dus4l, paics, pnp5a, prps1a*	**Thyroid function** *dio3b*
	Glycosylation *alg2, dpm1, gpaa1, nus1, pgap2*	
	Gluconeogenesis *gapdh, gapdhs, pfkfb3, pkma*	
	Extracellular matrix *fn1b, lamb1b, vtnb*	
	Mitochondrial function *atp5l, ckmt2a, mrps30, nfu1, suclg1, tomm6*	

Red, increased gene expression. Blue, reduced gene expression.

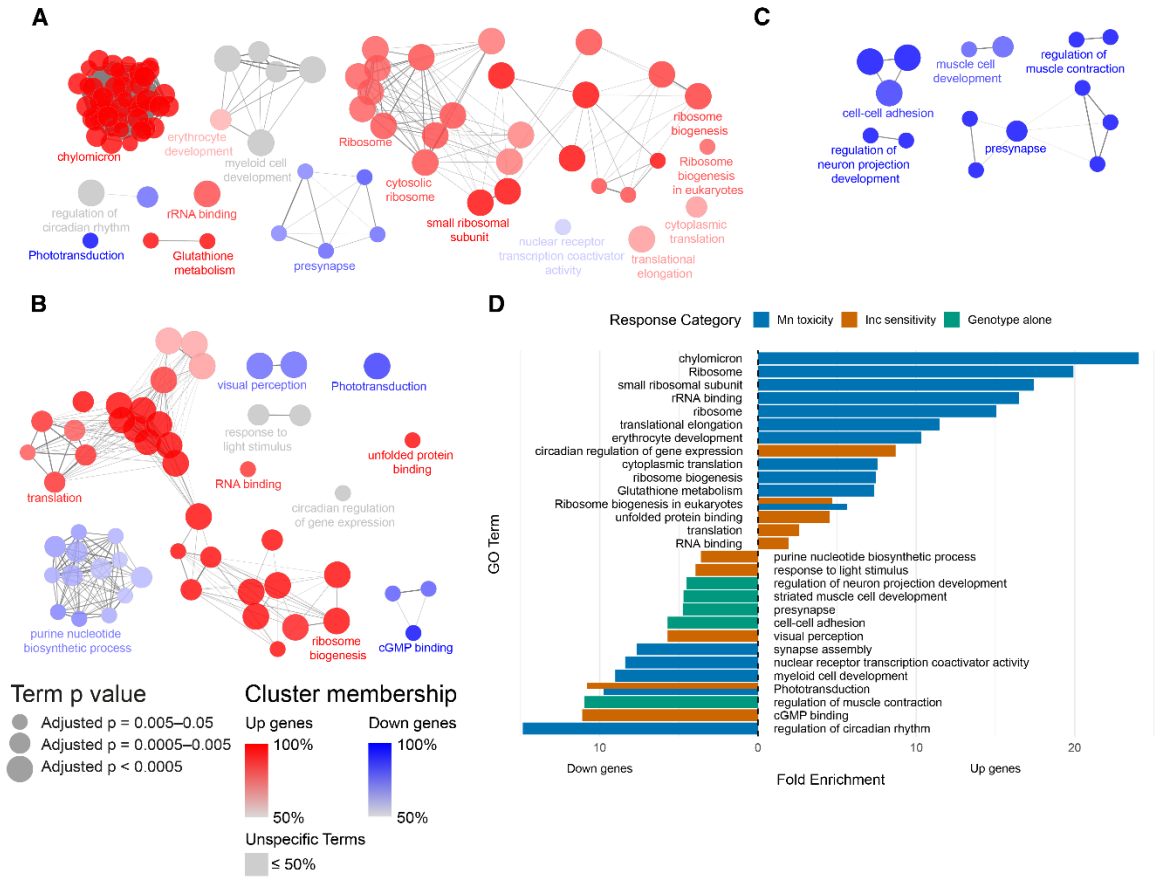

Fig. S1. Contribution to up- and down-regulated genes to GO enrichments.

(A-C) ClueGO network diagrams corresponding to the diagrams shown in Fig. 2C, 3G and 5E. Nodes represent enriched GO terms and edges connect nodes that share annotations to the significant genes. Each node is coloured according to the percentage of up/down-regulated genes contributing to the enrichment. Nodes coloured red have > 50% of the genes responsible for the enrichment upregulated, whereas blue nodes have > 50% of the genes downregulated. If the contribution of up/down-regulated genes is equal the nodes are grey. (A) Mn toxicity, (B) Increased sensitivity, (C) Mutant effect. (D) Bar chart showing the same information. The x-axis represents the Fold enrichment, [(genes in study set annotated to term / genes in study set) / (genes in reference set annotated to term / genes in reference set)]. Enrichment caused by upregulated genes are plotted to the right, whereas ones caused by downregulated genes are plotted to the left. blue = enrichments for the Mn toxicity set, orange = enrichments for the Increased sensitivity set, green = enrichments for the Mutant effect set.

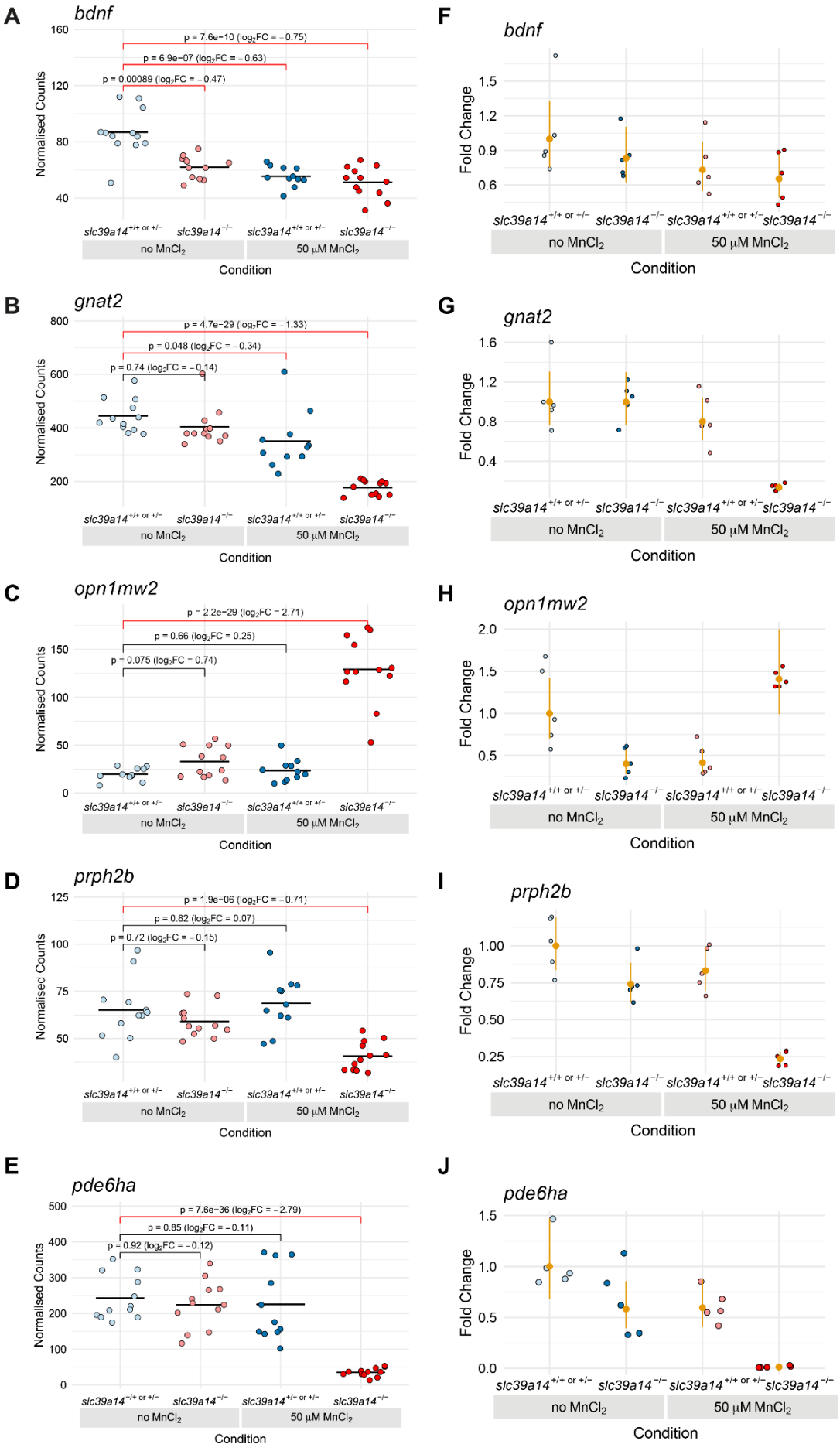
A
bdnf
p = 7.6e−10 (log2FC = −0.75)
p = 6.9e−07 (log2FC = −0.63)
p = 0.00089 (log2FC = −0.47)
Normalised Counts
slc39a14+/+ or +/−
slc39a14−/−
no MnCl2
50 μM MnCl2
Condition
F
bdnf
Fold Change
B
gnat2
p = 4.7e−29 (log2FC = −1.33)
p = 0.048 (log2FC = −0.34)
p = 0.74 (log2FC = −0.14)
G
gnat2
C
opn1mw2
p = 2.2e−29 (log2FC = 2.71)
p = 0.66 (log2FC = 0.25)
p = 0.075 (log2FC = 0.74)
H
opn1mw2
D
prph2b
p = 1.9e−06 (log2FC = −0.71)
p = 0.82 (log2FC = 0.07)
p = 0.72 (log2FC = −0.15)
I
prph2b
E
pde6ha
p = 7.6e−36 (log2FC = −2.79)
p = 0.85 (log2FC = −0.11)
p = 0.92 (log2FC = −0.12)
J
pde6ha

Fig. S2. qRT-PCR produces consistent results with transcriptome sequencing.

(A–D) Plots of the normalised counts for each sample for the genes *bdnf*, *gnat2*, *opn1mw2* and *prph2b*. Unexposed sibling embryos are light blue and $MnCl_2$ exposed ones are dark blue. Unexposed mutants are coloured light red and exposed mutants are dark red.

(E–H) Plots showing the qRT-PCR data for genes *bdnf*, *gnat2*, *opn1mw2* and *prph2b*. Values for individual samples are displayed as fold change relative to the mean value for unexposed siblings with the same colour scheme as in A–D. The mean and 95% confidence intervals for each condition are in orange.

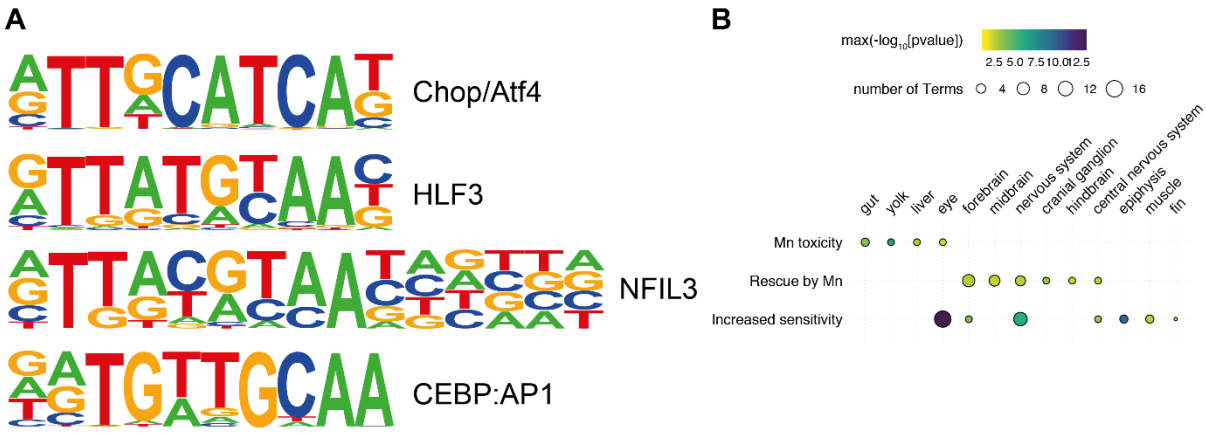

Fig. S3. Comparative analysis of gene sets.

(A) Example consensus binding motifs enriched in the promoters of genes that show increased sensitivity to Mn treatment in *slc39a14*$^{-/-}$ mutants (Group 1). The height of each base represents its frequency at that position in the consensus motif.

(B) Bubble plot of the ZFA enrichment results across the three categories of response. Individual enriched ZFA terms were aggregated to the tissue/organ level. For example, the terms optic cup, retina and photoreceptor cell are aggregated to the parent term eye. The size of each circle represents the number of individual terms enriched for the particular organ or tissue, and they are coloured by the smallest of the p values (-$\log_{10}$ scaled).

Table S1. List of differentially expressed genes identified by DeTCT and grouped by Mn toxicity (differentially expressed in $MnCl_2$ exposed siblings compared with unexposed siblings), Increased sensitivity (differentially expressed in $MnCl_2$ exposed mutants compared with unexposed siblings, but not differentially expressed in unexposed mutants compared to unexposed siblings or exposed siblings compared with unexposed siblings) and Mutant effect (differentially expressed in unexposed mutants compared with unexposed siblings). Also included are genes differentially expressed in unexposed heterozygotes compared with unexposed wild-type embryos (het_noMnCl2_vs_wt_noMnCl2) and ones differentially expressed in exposed heterozygotes compared with exposed wild-type embryos (het_MnCl2_vs_wt_MnCl2). Genes highlighted in mustard are further discussed in the manuscript. Available at Figshare: https://dx.doi.org/10.6084/m9.figshare.19550899

Table S2. List of the 10 most highly up- and downregulated genes per group (Mn toxicity, Increased sensitivity and Mutant effect).

	gene	p-value	log2 fold change	GO term	
Mn toxicity					
up					
1	fads2	2.77E-07	1.80	fatty acid biosynthesis	
2	lonrf1l	2.02E-18	1.53	metal ion binding	
3	cry1bb	5.08E-14	1.44	circadian rhythm	
4	eevs	1.47E-10	1.38	lyase activity	
5	lonrf1	5.64E-16	1.25	metal ion binding	
6	ptgdsb.1	2.33E-21	1.24	prostaglandin	
7	apoa4b.2	4.37E-05	1.15	chylomicron	
8	fech	1.32E-11	1.11	erythrocyte development	
9	apoa4a	0.000111	1.09	chylomicron	
10	soul5	3.83E-10	1.00	erythrocyte development	
down					
1	nr1d4b	7.52E-16	-1.15	circadian rhythm	
2	dre-mir-132-2	2.3E-06	-1.15	miRNA	
3	dspa	9.43E-05	-0.99	cell-cell adhesion	
4	sv2a	8.77E-06	-0.95	synapse, transmembrane transport	
5	creb5b	5.95E-06	-0.93	transcription, metal ion binding	
6	sncb	3.86E-06	-0.85	dopaminergic	
7	TMEM151A	0.000181	-0.83	membrane	
8	nfil3-6	2.53E-05	-0.80	circadian rhythm	
9	large2	4.19E-05	-0.77	protein glycosylation	
10	cipca	1.86E-05	-0.76	circadian rhythm	
Increased sensitivity					**additive/synergistic**
up					
1	opn1mw2	1.07E-27	2.46	phototransduction	synergism
2	hspa5	1.91E-32	1.63	protein folding	synergism
3	faim2b	1.12E-13	1.60	autophagy	synergism
4	ptpdc1b	4.03E-06	1.60	protein dephosphorylation	additive
5	zwi	0.000101	1.53	myelin sheath	additive
6	fbxo21	0.005509	1.50	DNA binding	additive
7	cst14b.1	0.002159	1.43	endopeptidase inhibitor	additive
8	atf3	3.02E-05	1.38	transcription	additive
9	wbp2	1.36E-08	1.36	transcription	synergism
10	gtpbp1	3.26E-15	1.32	translational elongation	synergism
down					
1	ctsll	3.17E-15	-4.89	proteolysis	synergism

2	pde6ha	2.1E-35	-2.68	phototransduction	synergism
3	cyp11c1	3.55E-10	-2.39	oxidoreductase, metal ion/heme binding	synergism
4	pde6ha	2.91E-11	-2.09	phototransduction	synergism
5	slc1a2a	3.2E-19	-1.96	symporter, glutamate	synergism
6	dre-mir-124-4	0.000506	-1.76	miRNA	additive
7	grk1b	2.28E-10	-1.73	phototransduction	synergism
8	guca1g	2.1E-08	-1.71	phototransduction	synergism
9	six4a	0.000352	-1.69	transcription	additive
10	guca1d	1.17E-07	-1.68	phototransduction	synergism
Mutant effect					**Mn rescue**
up					
1	pxmp2	0.000741	1.17	peroxisomal membrane	not rescued
2	aacs	9.61E-07	1.16	fatty acid metabolism	not rescued
3	ddx1	0.000861	0.90	RNA helicase	rescued
4	mtmr12	0.000708	0.87	phosphatidylinositol dephosphorylation	rescued
5	sqstm1	0.000455	0.67	autophagy, metal ion binding	not rescued
6	alas1	7.52E-08	0.65	heme biosynthetic process	not rescued
7	dio3b	2.76E-05	0.62	thyroxine 5-deiodinase activity	not rescued
8	wdr44	0.000126	0.62	small GTPase binding	rescued
9	crebrf	0.000825	0.56	transcription, UPR	rescued
10	ces3	0.000236	0.55	hydrolase activity	rescued
down					
1	ebf3a	2.19E-06	-1.87	transcription, metal ion binding	rescued
2	klhl24b	0.000628	-1.62	glutamate receptor	rescued
3	pcdh7b	1.04E-05	-1.57	membrane, calcium ion binding	rescued
4	fam120c	4.07E-05	-1.55	nucleus	rescued
5	clec3ba	8.74E-05	-1.55	bone mineralization	rescued
6	ptprga	1.18E-06	-1.52	protein dephosphorylation	rescued
7	bmp7b	0.000316	-1.47	BMP signaling pathway	rescued
8	sv2a	8.11E-12	-1.46	synapse, transmembrane transport	rescued
9	phip	2.98E-05	-1.46	transcription	rescued
10	syt6a	4.21E-05	-1.46	synapse, calcium-ion regulated exocytosis	rescued

Table S3. List of the 10 most significantly differentially expressed genes with highest p-values for each group (Mn toxicity, Increased sensitivity and Mutant effect).

	gene	p-value	log2 fold change	GO term	
Mn toxicity					
1	sv2a	0.000864522	-0.95	Calcium, presynaptic neurotransmitter release	
2	igsf9ba	6.33E-05	-0.75	Cell adhesion, nervous system development	
3	sgcd	0.043419419	-0.68	Muscle	
4	CTBP1	0.01601469	-0.35	Transcription regulation	
5	dla	0.007417209	-0.42	Calcium, neurogenesis, notch	
6	parn	0.010107324	-0.37	Metal binding, mRNA degradation	
7	efnb2a	0.011782537	-0.36	Ephrin receptor binding, cell adhesion, axon guidance	
8	smurf2	0.008605029	-0.70	E3 ubiquitin-protein ligase, protein ubiquitination	
9	alas1	0.00084604	0.55	heme biosynthesis, response to hypoxia	
10	skib	0.000942987	-0.59	transcription factor, SMAD binding	
	gene	p-value	log2 fold change	GO term	
Increased sensitivity					additive/ synergistic
1	pde6ha	3.36859E-31	-2.68	Phototransduction	synergism
2	hspa5	1.53395E-28	1.63	Unfolded protein response	synergism
3	opn1mw2	5.72801E-24	2.46	Phototransduction	synergism
4	atp1a1b	1.27919E-16	0.95	Sodium/potassium-transport, metal binding	synergism
5	slc1a2a	7.34528E-16	-1.96	Excitatory amino acid transporter, glutamate reuptake	synergism
6	xbp1	7.34528E-16	0.84	Unfolded protein response	synergism
7	opn1mw1	1.91042E-14	-0.95	Phototransduction	synergism
8	rcvrna	3.81359E-14	-1.25	Phototransduction, calcium binding	synergism
9	slc1a2b	3.81359E-14	0.55	Excitatory amino acid transporter, glutamate reuptake	synergism
10	stm	6.39958E-13	0.63	Calcium ion transport, ephrin and notch receptor signalling	synergism
Mutant effect					Mn rescue
1	igf2bp2b	4.87E-14	-1.26	Translation regulation	rescued
2	gnai2a	2.96E-09	-0.70	G protein-coupled receptor signaling pathway, metal binding	rescued
3	anp32a	1.52E-08	-0.74	Apoptosis, RNA binding	rescued
4	sv2a	2.96E-08	-1.46	Calcium, presynaptic neurotransmitter release	rescued

5	adgrl1a	1.05E-07	-1.31	G protein-coupled receptor activity, cell adhesion	rescued
6	strn4	1.36E-07	-1.09	Calcium, calmodulin binding	rescued
7	igsf9ba	1.98E-07	-0.97	Cell adhesion, nervous system development	rescued
8	pcdh2aa15	5.7E-07	-0.68	Calcium ion binding, cell adhesion	rescued
9	ace2	1.58E-06	-0.88	Metal binding, angiotensin maturation	rescued
10	CU929544.1	1.58E-06	-0.48	Receptor-type tyrosine-protein phosphatase delta-like	rescued

Table S4. List of enriched Gene Ontology (GO) terms. Available at Figshare:

https://dx.doi.org/10.6084/m9.figshare.19550932

Table S5: Statistical analysis of qRT-PCR data. Available at Figshare:

https://dx.doi.org/10.6084/m9.figshare.19550938

Table S6: Enrichment of zebrafish anatomy (ZFA) terms. Available at Figshare:

https://dx.doi.org/10.6084/m9.figshare.19550959

Table S7. Locomotor activity data. Available at Figshare:

https://dx.doi.org/10.6084/m9.figshare.19550965

Table S8. HOMER enrichment analysis of transcription factor motifs. Available at Figshare:

https://dx.doi.org/10.6084/m9.figshare.19550968

Table S9. Optokinetic response data. Available at Figshare:

https://dx.doi.org/10.6084/m9.figshare.19550986

Table S10. HCR *in situ* hybridisation probes.

Target mRNA	***gad1b***
Amplifier	B1
Fluorophore	Alexa 488
Initiator I1	Initiator I2
gAggAgggCAgCAAACggAA	TAgAAgAgTCTTCCTTTACg
Probe sequences	
Pair1	Pair2
AACAGTGGGACATATCCCTTCTGTT	ACTGTAGTACCCGCCGTGGCATTCA
AAGCGCTCATTGTTGTCGCACGACA	TTGGAGAAATCTGTCTCATCGCGCG
CTATATGTCGTAAGGTGACTGTGTA	ACAAGCACCGGCTGTTATCCCAATG
GCGTGATTGGAGACCACCATTCGGA	AGGAAATCGATGTCCGACTTGGTGA
GCGGGCAGTAGATCTCGCGCGAACA	TGGATTGTGGGCTCCTCGCCGTTTT
AGAAAGGGGCTTTGTTAAAAGGGTG	GTTTACACACAGACCCCACTATTAC
TTTGGCCAGCCGATGATCTCCCGCA	GGTGAGAAGAGCGCATCTCCATCTC
CACGCACCATCCACATGTAACCACA	TTTCTGGACATCAACAGTCCTCCAC
AAATATTTATACCGCGCAACCATCA	GACATGCCTTTGGTTTTGACTTCAG
CAGACTGAATGGAAAAATCTGACAC	AGTCCACGGGAAACACCTCAATGCT
TTCTCTCTGACCAGGATGGCTGAAC	ATGGAGTTGCAGCCCTGCAGAATGC
Target mRNA	**cfos**
Amplifier	B3
Fluorophore	Alexa 546
Initiator I1	Initiator I2
gTCCCTgCCTCTATATCTTT	TTCCACTCAACTTTAACCCg
Probe sequences	
Pair1	Pair2
TGCACCGGGAAGACGCGTCGCAGTC	CGCTGTCGCCGCTCGGTGAAGCCGT
TGCTGCCCCTGCGATGCACTGATGT	AGGAGTCGGACGACTGATCGTTGCT
CACGTCGACGGTTGCGGCATTTCGC	TTTCAGCTTGCAGTGTATCGGTGAG
AGGTAGTGACGATCTCTGGGACTGA	ATGTGTTTGGTGTGGAAGAGACCAC
TGCAGATGGGTTTGTGTGCGGCGAG	CTGGGAAGCTGGCGTCGGCCGGGAT
CAGAGGAGATCATGGGCTGGACCAT	ATTGAGCTGCGCCGTTGGAGGGCGC
AGGCTGGAGTGCAGGTGACGACGGG	ACATGAAGGAAGACGTGTAGGTGGT
GCGCTAATATATCCAGAAAGTTAAA	CAAAAGTCGAAAAGCACGAGCTATC

Table S11. Download links for sequence data at the European Nucleotide Archive. Available at Figshare: https://dx.doi.org/10.6084/m9.figshare.19550989